Mon. Not. R. astr. Soc. (1991) **253**, 710–726

The velocity dispersion anisotropy and mass-to-light ratio of elliptical galaxies

Roeland P. van der Marel
Sterrewacht Leiden, Postbus 9513, 2300 RA Leiden, The Netherlands

Accepted 1991 August 1. Received 1991 August 1; in original form 1991 May 13

SUMMARY

Axisymmetric dynamical models are constructed for 37 bright elliptical galaxies for which high-quality photometrical, and both major and minor axis kinematical data are available in the literature. The models are of the type used previously by Binney, Davies & Illingworth and van der Marel, Binney & Davies. The projected kinematics are predicted from the observed surface photometry, assuming a constant mass-to-light ratio, and a velocity ellipsoid with $\sigma_r = \sigma_\theta$ [i.e. $f = f(E, L_z)$].

For the sample as a whole it is found that these models tend to predict too much motion on the major axis. This implies that elliptical galaxies as a class must have $\sigma_r > \sigma_\theta$, which has not been demonstrated before. This result is consistent with general expectation as based on *N*-body simulations of dissipationless collapse.

From the models accurate mass-to-light ratios are derived that are corrected for the effects of rotation and radial anisotropy. The average mass-to-light ratio for the galaxies in the sample is $(M/L)_B = (5.93 \pm 0.25) h_{50}$. The mass-to-light ratios correlate with total luminosity according to $(M/L) \propto L^{0.35 \pm 0.05}$. The quantity $(v/\sigma)^*$ is identified as a second parameter in this relation. Galaxies with high $(v/\sigma)^*$ tend to have a low mass-to-light ratio (for their luminosity).

The observed velocities in the outer parts of the galaxies in the sample systematically exceed the velocities predicted by our (constant mass-to-light ratio) models. From this it is argued that no *axisymmetric* constant mass-to-light ratio models can fit the kinematical data in the outer parts of elliptical galaxies. Either dark haloes must be present, or more detailed *triaxial* models must be studied.

1 INTRODUCTION

Binney (1978) and Davies *et al.* (1983) used the tensor virial theorem to demonstrate that elliptical galaxies are not flattened by rotation, but by the anisotropy of their velocity dispersion tensor. In the present paper it is studied what the sense of this anisotropy is ('radial' or 'tangential'). The answer to this question is important since it can yield constraints on mechanisms for galaxy formation. The end-products of *N*-body simulations in which a spherical configuration collapses dissipationlessly are radially anisotropic in their outer parts (van Albada 1982). Several authors have constructed distribution functions for elliptical galaxies, that reproduce this property (e.g. Bertin & Stiavelli 1984; Merritt 1985). It is of great interest to study if observations indeed support this idea.

Since elliptical galaxies are not flattened by rotation there is no reason why they should be axisymmetric. Indeed it is by now well-established that elliptical galaxies are in general triaxial (see the review of de Zeeuw & Franx 1991). Isophote twists and minor-axis rotation are generally interpreted as evidence for triaxiality. However, it is in general not possible to determine the intrinsic shape of an individual galaxy. In the last decade several authors have tried to determine the distribution of intrinsic shapes of elliptical galaxies by studying the observed distribution of the parameter $\mu \equiv v_{min}/v_{maj}$, the most recent effort being that of Franx, Illingworth & de Zeeuw (1991, hereafter FIZ). Unfortunately, this problem is highly degenerate, and many distributions of (triaxial) intrinsic shapes fit the data equally well. FIZ demonstrate that the *mean* triaxiality of elliptical galaxies is not very large; even a distribution with ~60 per cent of all elliptical galaxies oblate and ~40 per cent prolate is not excluded by the observations.

In elliptical galaxies one sees along every line of sight the projection of a mixture of the principal velocity dispersion components. To discriminate between different dynamical models with different velocity distributions, it is thus

required to compare model predictions to kinematical observations on *both* the major *and* the minor axis separately (Fillmore 1986), which is what is done in the present paper. As there is at present little hope of determining simultaneously, both the distribution of intrinsic shapes of elliptical galaxies, as well as the shape of their velocity ellipsoids, we restrict ourselves in this paper to axisymmetric models. From the tensor virial theorem it follows that $\frac{1}{2}\langle \overline{v_R^2}+\overline{v_\phi^2}\rangle/\langle \overline{v_z^2}\rangle > 1$ for oblate galaxies, and $\frac{1}{2}\langle \overline{v_R^2}+\overline{v_\phi^2}\rangle/\langle \overline{v_z^2}\rangle < 1$ for prolate galaxies, where $\langle\cdot\rangle$ denotes the mass-weighted average over the system. The problem then reduces to the question as to whether radial pressure or azimuthal pressure is mainly responsible for the pressure of the system parallel to the equatorial plane. Both models in which $f=f(E,L_z)$, and models in which $f=f(E,L_z,I_3)$ are possible. In the first type of model one always has $\sigma_R=\sigma_z$. The requirements of the tensor virial theorem are then satisfied by having $\langle \overline{v_\phi^2}\rangle^{1/2} > \langle\sigma_R\rangle = \langle\sigma_z\rangle$ in the oblate case, or the other way round in the prolate case. In the second type of model one can have that both $\langle \overline{v_\phi^2}\rangle^{1/2} > \langle\sigma_z\rangle$ and $\langle\sigma_R\rangle > \langle\sigma_z\rangle$ in the oblate case, or the other way round in the prolate case.

In the present paper a sample of 37 elliptical galaxies is studied, for which high-quality photometrical and kinematical data have been published in recent years. For these galaxies one-component axisymmetric models with $\sigma_r=\sigma_\theta=\sigma_R=\sigma_z$ [i.e., $f=f(E,L_z)$] are constructed. Both oblate and prolate models are studied. The models are of the type devised by Binney, Davies & Illingworth (1990, hereafter Paper I), who applied their model to three E3/E4 galaxies. Subsequently van der Marel, Binney & Davies (1990, hereafter Paper II) extended and refined parts of the model and applied it to four E1/E2 galaxies. For NGC 720 (Paper I) conclusive evidence was found for radial anisotropy ($\sigma_r > \sigma_\theta$). However, even from the combined results of Paper I and Paper II it is not clear whether or not this is also true for elliptical galaxies in general. The large sample studied here enables a detailed study of this question. Apart from the models a simple argument is presented, based on the tensor virial theorem. For those galaxies that are not well fitted by the model, this argument is used to estimate the range of velocity ellipsoid shapes that will provide a good fit.

In fitting the models to the data a mass-to-light ratio is derived that incorporates the effects of rotation and velocity dispersion anisotropy, and is obtained by fitting to the major and minor axis kinematical profiles, and not just to core or global kinematical properties. These mass-to-light ratios are thus much more accurate than values obtained from either core fitting or (tensor) virial theorem formulae. The mass-to-light ratios are examined for correlations with other global properties.

The models are also used to examine the available data for evidence on the presence of dark haloes in ellipticals. For elliptical galaxies evidence on the presence of dark haloes is still rather marginal, in contrast to the case of spiral galaxies, where H I rotation curves can be measured far beyond the optical disc. A review on this subject is given by de Zeeuw (1991).

The paper is organized as follows. Section 2 describes the model and Section 3 the sample. Section 4 discusses the results of fitting the models to the data. Conclusions are presented in Section 5. The predictions and the data for several individual galaxies are plotted in Appendix B. In Appendix A and Appendix C some auxiliary formulae are derived.

2 THE MODEL

The model* predicts the kinematics of an elliptical galaxy from its observed surface photometry. The model is based on three assumptions: (i) axisymmetry; (ii) constant mass-to-light ratio; and (iii) $\sigma_r=\sigma_\theta$ [i.e. $f=f(E,L_z)$]. The validity of these assumptions is assessed by comparing the predictions to the observations.

The surface photometry is deprojected to a three-dimensional luminosity density for a fixed assumed inclination angle i (being the angle between the symmetry axis and the line of sight) using Lucy iteration. Both oblate and prolate models are possible. The mass density is calculated by assuming a constant mass-to-light ratio Υ. The potential is calculated from the Poisson equation. Because of assumption (iii), the Jeans equations of hydrostatic equilibrium are a closed set, which is solved for the two unknowns $\overline{v_\phi^2}$ and $\sigma^2 \equiv \sigma_r^2 = \sigma_\theta^2$. For every point on the sky the root mean square (rms) projected line-of-sight velocity $[\![\overline{v_l^2}]\!]^{1/2}$ is calculated, which is compared to the observations; v_l is the component of the velocity along the line of sight and $[\![\cdot]\!]$ denotes the luminosity-weighted projection along the line of sight. The quantity $[\![\overline{v_l^2}]\!]^{1/2}$ is related to the observed streaming velocity v and the observed velocity dispersion $\hat{\sigma}$ by

$$[\![\overline{v_l^2}]\!]^{1/2} = \sqrt{v^2+\hat{\sigma}^2}. \tag{1}$$

To compare the predictions of the model to the observed v and $\hat{\sigma}$ separately, one needs to specify how $\overline{v_\phi^2}$ splits into streaming motion and azimuthal velocity dispersion. For oblate galaxies this is conveniently done by introducing a parameter k, such that

$$\overline{v}_\phi^2 = k^2(\overline{v_\phi^2}-\sigma^2). \tag{2}$$

For prolate galaxies in general $\overline{v_\phi^2} < \sigma^2$, there is no natural way of assigning part of $\overline{v_\phi^2}$ to rotation, and the parameter k is not used.

Also calculated from the predictions of the model† is the function $\nu(r)$, defined such that

$$\nu^2(r) \equiv [\![\overline{v_l^2}]\!]_{maj}(r)/[\![\overline{v_l^2}]\!]_{min}(r), \tag{3}$$

where r (in arcsec) is the galactocentric distance on the sky.‡ This function is a useful diagnostic of the velocity ellipsoid structure, since on the major and the minor axis one sees different components of the velocity dispersion tensor. Note that $\nu(r)$ depends on the inclination i only, and not on Υ and k.

* For a *detailed* description of the model, the reader is referred to Paper I and Paper II.

† This was not done in Paper I and Paper II.

‡ One could also have defined, instead of $\nu(r)$, a quantity that is the ratio of the rms projected line-of-sight velocity calculated in points on the major and minor axis that lie on the same isophote. This however is only a sensible definition if the contours of constant surface brightness and of constant rms projected line-of-sight velocity are the same. From Fillmore (1986) this is known not to be the case.

2.1 Estimating v using the tensor virial theorem

To get some understanding of what exactly is measured by $v(r)$, a simple estimate of this quantity is presented in this section, based on the tensor virial theorem, which states that for a spheroidal system (e.g. Binney 1978)

$$\tfrac{1}{2}(\langle\overline{v_\phi^2}\rangle+\langle\overline{v_R^2}\rangle)/\langle\overline{v_z^2}\rangle=\Omega, \tag{4}$$

where Ω is a function of the axial ratio q_t of the mass-density only, and is given in Appendix A. In a spherical stellar system the velocity ellipsoid everywhere aligns with spherical coordinate axes, i.e. $\overline{v_r v_\theta}=0$. In a flattened system this is not necessarily the case. However, it seems a reasonable assumption that also in this case $\overline{v_r v_\theta}=0$ (e.g. Bacon 1985). The only non-zero second-order velocity moments are then σ_r^2, σ_θ^2 and $\overline{v_\phi^2}$. To obtain an estimate v_{tvt} for v without explicitly solving the Jeans equations, one has to make some assumption about the behaviour of these second-order velocity moments as a function of position in the galaxy. Here the very naive assumption is made that σ_r^2, σ_θ^2 and $\overline{v_\phi^2}$ all three have a *constant* (but different) value. (This means that in every point $\overline{v_\phi^2}=\langle\overline{v_\phi^2}\rangle$, etc.) If the mass density is of the form

$$\rho(R,z)=\rho_0(q_t^2R^2+z^2)^{-s/2}, \tag{5}$$

then

$$\overline{v_R^2}=\overline{v_r^2}+\eta(\overline{v_\theta^2}-\overline{v_r^2}), \qquad \overline{v_z^2}=\overline{v_\theta^2}+\eta(\overline{v_r^2}-\overline{v_\theta^2}), \tag{6}$$

where η is a geometrical factor that depends on q_t and s only, and is given in Appendix A. If the mass-to-light ratio of the galaxy is constant, then the line-of-sight projections for an oblate system are

$$[\overline{v_l^2}]_{min}=\overline{v_\theta^2}+\alpha(\overline{v_r^2}-\overline{v_\theta^2}), \tag{7a}$$

$$[\overline{v_l^2}]_{maj}=\overline{v_\theta^2}+\beta(\overline{v_\phi^2}-\overline{v_\theta^2})+\gamma(\overline{v_r^2}-\overline{v_\theta^2}), \tag{7b}$$

and the other way round (exchange 'min' and 'maj') for a prolate system. Here α, β and γ are geometrical factors that depend on q_t, the assumed inclination i, and s. Expressions for α, β and γ are given in Appendix A. By analogy to the work of Binney (1980) a parameter

$$B\equiv 1-(\sigma_\theta^2/\sigma_r^2), \tag{8}$$

is introduced, that measures the radial anisotropy of the galaxy. Combining the above expressions yields

$$v_{tvt}^2=\frac{1+2\beta(\Omega-1)+B\{\gamma-1+\beta[2\Omega(\eta-1)+\eta+1]\}}{1+B(\alpha-1)}, \tag{9}$$

for oblate systems, and the reciprocal of this expression for prolate systems. For fixed axial ratio q_a on the sky and fixed inclination angle i, the true axial ratio q_t of the galaxy is determined by (Mihalas & Binney 1981, equation 5-21)

$$q_t^2\sin^2 i+\cos^2 i=\begin{cases}q_a^2 & (q_t<1)\\ 1/q_a^2 & (q_t>1)\end{cases}. \tag{10}$$

Therefore, for fixed s, v_{tvt} is a function $v_{tvt}(q_a,i,B)$ only. This function does not depend on r because there is no scale in either the assumed mass density or the assumed dynamical structure. The estimate v_{tvt} captures the essence of the influence of intrinsic flattening, velocity dispersion anisotropy and inclination and projection effects on v. It can thus provide useful *qualitative* insight into the results of our models. However, the estimate v_{tvt} must not be used in a *quantitative* manner, since the internal dynamical structure of the system has been totally neglected. In an oblate system with $f(E,L_z)$ for example, $\overline{v_\phi^2}>\sigma_\theta^2$ in the equatorial plane, but $\overline{v_\phi^2}=\sigma_\theta^2$ near the symmetry axis, because of continuity requirements. The influence of such effects on v is not captured in v_{tvt}.

The function $v_{tvt}(q_a,i,B)$ is plotted in Fig. 1(a) (oblate) and 1(b) (prolate). Note that there is no large dependence on s. For oblate models v_{tvt} decreases with increasing q_a (for fixed i and B) since rounder galaxies have less azimuthal motion

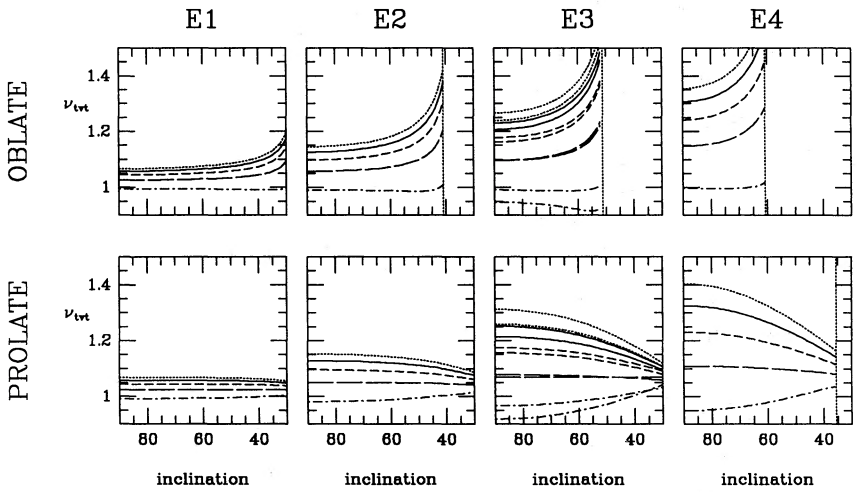

Figure 1. Plotted is the function $v_{tvt}(q_a,i,B)$ for four different apparent axial ratios on the sky (expressed in terms of the corresponding Hubble type), as a function of the assumed inclination i. Curves are plotted for $B=-0.25$ (dotted), $B=0$ (solid), $B=0.25$ (short dash), $B=0.5$ (long dash) and $B=0.75$ (short dash-dot), and were calculated for $s=3$ in equation (5). In the plots for E3 the corresponding curves for $s=4$ are also plotted for comparison. (a) (upper panel) Oblate models. The dotted vertical lines indicate the inclination angle for which $q_t=0.4$. Only very few ellipticals are this flat. (b) (lower panel) Prolate models. The dotted vertical lines indicate the inclination angle for which $q_t=2.5$.

(which is seen mainly on the major axis). Similar reasoning explains why v_{tvt} decreases with increasing B (for fixed q_a and i). For prolate models v_{tvt} also decreases with increasing B (for fixed q_a and i), since galaxies with small B have depressed azimuthal velocities that are seen mainly on the minor axis. In Section 4.1 the estimate $v_{tvt}(B=0)$ is compared to the results of our models, and it is demonstrated that v_{tvt} is indeed a useful estimate. Two important conclusions can be drawn from Fig. 1.

(i) For oblate galaxies $v_{tvt}(B=0)$ has a minimum for $i=90°$. Therefore, if for a particular galaxy the predicted $v(r)$ of the oblate model with $i=90°$ exceeds the observations, it can be concluded that this galaxy cannot have $f=f(E,L_z)$, but must have some radial anisotropy ($B>0$).

(ii) For prolate galaxies $v_{tvt}(B=0)$ has a maximum for $i=90°$ (i.e. broadside on). Therefore, if for a particular galaxy the predicted $v(r)$ lies between unity and this maximum, there are two possibilities: either the galaxy is radially anisotropic ($B>0$) and close to broadside-on, or $\sigma_r \approx \sigma_\theta (B \approx 0)$ and the galaxy is closer to end-on. In the latter case the galaxy must be intrinsically rather elongated.

3 THE SAMPLE

3.1 Sample selection

The model requires high-quality surface photometry and kinematical data (both dispersion and rotation profiles) on both the major and the minor axis. The more restrictive of these requirements is that the kinematical data must be available. The kinematical data are taken from the work of Davies & Birkinshaw (1988, hereafter DB), Jedrzejewski & Schechter (1989, hereafter JS) and Franx, Illingworth & Heckman (1989a, hereafter FIHa). To these data were added the data presented in Paper I. The surface photometry is sought in the CCD studies of Djorgovski (1985, hereafter Dj), Jedrzejewski (1987, hereafter Je), Franx, Illingworth & Heckman (1989b, hereafter FIHb), and Peletier *et al.* (1990, hereafter PDIDC). Galaxies for which no CCD surface photometry could be found, for which no dispersion profiles are available, or for which the available kinematical data are not along the major and the minor axis, were not included in the sample. The resulting sample consists of 37 galaxies, and is neither complete nor homogeneous. Basic properties are listed in Table 1. There are not many flat galaxies in the sample, since most galaxies were selected by the original authors with the aim of finding minor axis rotation, which is more likely in apparently round ellipticals.

Oblate models are constructed for all the galaxies in the sample. Since the oblate models always predict $v_{min}=0$, prolate models (that have $v_{maj}=0$) are also constructed for the five galaxies in the sample that have $v_{min}>v_{maj}$. These galaxies are labelled 'm' in column (13) of Table 1. Two of these galaxies (NGC 4406 and NGC 7626), and four of the remaining galaxies (NGC 1439, NGC 3608, NGC 4494 and IC 1459) have a peculiar rotation curve (e.g. counter-rotating or kinematically misaligned core). NGC 4406 probably rotates around its long axis in the outer parts (FIZ). For those galaxies that either have $v_{min}>v_{maj}$ or a peculiar rotation curve, no attempt is made to fit the parameter k. Eight galaxies in the sample have an isophote twist $\gtrsim 20°$ between 5 and 50 arcsec (NGC 636, NGC 1379, NGC 1395, NGC 1549, NGC 4486, NGC 4494, NGC 7144 and NGC 7145). The results for these galaxies must be interpreted with care since for them the assumption of intrinsic axisymmetry cannot be correct.

3.2 The surface photometry

The surface photometry (surface brightnesses, ellipticities and $\cos 4\theta$ deviations) is interpolated onto a grid as described in Paper II. All surface brightnesses are transformed to the Johnson R-band. Special attention is paid to the inner few arcsec, where seeing effects are important. PDIDC have calculated radii R_Σ and R_ε (expressed in terms of the effective radius r_e, and depending on the FWHM of the seeing), beyond which the error in the surface brightness due to seeing $\Delta\Sigma < 0.05$ mag, and beyond which the error in the ellipticity due to seeing $\Delta\varepsilon < 0.02$. For all the galaxies in the sample R_Σ and R_ε are calculated, typical values being 3 and 6 arcsec, respectively. PDIDC show that the apparent decrease in ellipticity towards the centre that is seen in many ellipticals can often be attributed to seeing effects only. Therefore ε is kept constant within R_ε to its value at R_ε. The same is done for the $\cos 4\theta$ deviations of the isophotes from ellipses. The surface brightness profile is cut off at R_Σ. Then a modified Hubble profile [$\rho(r) \propto cst$ for $r \to 0$), a Hernquist model [$\rho(r) \propto r^{-1}$ for $r \to 0$], and a Jaffe model [$\rho(r) \propto r^{-2}$ for $r \to 0$] are least-squares fitted to the surface brightnesses between R_Σ and 10 arcsec. Of these three fits, the one that provides the best fit is chosen to extrapolate the surface brightnesses onto the grid from R_Σ inward. The Lucy iterations are started using as initial guess the flattened ($r^2 \to q^2R^2 + z^2$) modified Hubble/Hernquist/Jaffe model§ that provides the best least-squares fit to all the data on the grid.

The kinematical predictions of the model are influenced by noise in the surface photometry, and the type of model used to extrapolate the data from R_Σ inwards.¶ The model was tested with pseudo surface photometry to estimate the size of these effects. This test is described and plotted in Fig. 2. Only inside ~4 arcsec do the predictions of the model depend on the type of extrapolation used in the inner parts. Henceforth, all predictions inside 4 arcsec are discarded. Beyond 4 arcsec the errors in the predictions are everywhere smaller than the typical observational errors (compare Fig. 2 to Appendix B).

The mass-to-light ratio derived by the model depends slightly on the extrapolation used in the inner parts. A Jaffe model has more mass in the central parts than does a Hernquist model, which in turn has more mass in the central parts than a modified Hubble model. This property of these

§ If the data are extrapolated from R_Σ inward using a *modified Hubble* model, then a flattened *modified Hubble* model is used to start the Lucy iteration from, etc. The possibility of starting the Lucy iteration from a Hernquist (1990) model was not used in Paper I and II.

¶ Rybicki (1987) has demonstrated that the deprojection of an axisymmetric body at $i<90°$ is not unique. This means that projection + deprojection is not necessarily the identity operation. For $i<90°$ this introduces additional errors into the kinematical predictions of the model. However, the results of a number of tests indicate that, at least for $i \gtrsim 60°$, these errors are insignificant (with respect to the observational errors).

Table 1. Properties of the galaxies.

Galaxy	Classification RC2	RSA	B_T	r_e	ϵ	c_4	D	M_B	μ_e	SP	Kin	v_{rot}	$\bar{\sigma}$
				"			Mpc					km/s	
(1)	(2)	(3)	(4)	(5)	(6)	(7)	(8)	(9)	(10)	(11)	(12)	(13)	(14)
NGC 0636	E3/E1	E1	12.33	21	0.15	0.9	30.0	-20.06	20.71	FIH	FIH	71	152
NGC 0720	E5/E3	E5	11.16	52	0.39	-0.3	41.0	-21.90	21.14	PD	BDI	56	226
NGC 0777	E1/E2	E1	12.37	30	0.15	-0.4	87.9	-22.35	21.60	Dj	JS	35	269
NGC 1052	E4/E2	E3/S0	11.28	37	0.30		34.5	-21.41	21.11	PD	BDI/DB	76	201
NGC 1379	E0	E0	11.66	43	0.03	0.2	28.4	-20.61	21.79	FIH	FIH	20	110
NGC 1395	E2/E3	E2	10.94	50	0.17	-1.4	39.8	-22.06	21.22	FIH	FIH	100	234
NGC 1399	E1P	E1	10.55	45	0.12	0.3	28.4	-21.72	20.68	FIH	FIH	27	292
NGC 1404	E1	E2	10.89	29	0.13	0.5	28.4	-21.38	20.02	FIH	FIH	90	245
NGC 1407	E0/E0	E0	10.57	74	0.05	-0.3	39.8	-22.43	21.85	FIH	FIH	47	257
NGC 1439	E1/E1	E1	12.07	43	0.09	-0.3	39.8	-20.93	22.15	FIH	FIH	11	136
NGC 1549	E0	E2	10.58	51	0.13	-0.5	24.3	-21.34	20.96	FIH	FIH	49	196
NGC 1600	E3/E2	E4	11.79	56	0.34	-1.0	80.4	-22.74	22.17	PD	JS	2	289
NGC 1700	E4/E1T	E3	12.26	16	0.27	1.3	62.8	-21.73	19.94	FIH	FIH	86	240
NGC 2749	E3/E2	E3	12.54	40	0.21		93.7	-22.32	22.27	Dj	JS	m90	223
NGC 3091	E3/E2	E3	12.09	35	0.25	-0.7	81.7	-22.47	21.52	Je	FIH	108	289
NGC 3379	E1/E1	E0	10.43	38	0.09	0.2	17.1	-20.74	20.16	PD	DB/FIH	50	196
NGC 3557	E3	E3	11.13	43	0.24	0.0	48.0	-22.28	21.01	Je	FIH	153	244
NGC 3608	E2/E3	E1	11.68	39	0.20	-0.3	39.8	-21.32	21.41	Je	JS	26	175
NGC 4261	E2/E2	E3	11.32	44	0.22	-1.7	55.7	-22.41	21.25	PD	DB	m112	310
NGC 4374	E1	E1	10.13	57	0.15	-0.5	26.7	-22.00	20.81	PD	DB	8	290
NGC 4406	E3/E3	$S0_1$/E3	9.87	101	0.20	-0.9	26.7	-22.26	21.65	PD	FIH	m39	226
NGC 4472	E2/E4	E1/$S0_1$	9.32	114	0.16	-0.4	26.7	-22.81	21.40	PD	DB/FIH	81	283
NGC 4486	E0P/E1	E0	9.52	106	0.04	0.0	26.7	-22.61	21.60	PD	DB	8	305
NGC 4494	E1-2/E1	E1	10.69	50	0.16	0.4	13.9	-20.03	20.97	Dj	JS	63	150
NGC 4636	E0/E1	E0/$S0_1$	10.20	117	0.08	-0.2	26.7	-21.93	22.23	PD	DB	17	199
NGC 4649	E2/E1	$S0_1$	9.77	82	0.15	-0.6	26.7	-22.36	21.10	PD	FIH	53	315
NGC 4697	E6/E4	E6	10.03	95	0.41	2.4	15.9	-20.97	21.41	PD	BDI	99	176
NGC 5198	E1/E2	E1	12.61	31	0.15		74.6	-21.75	21.89	Dj	JS	4	181
NGC 5846	E0/E0	S0	10.67	49	0.07		46.7	-22.68	22.25	Dj	FIH	2	230
NGC 7144	E0	E0	11.75	41	0.03	0.3	36.9	-21.08	21.78	FIH	FIH	36	157
NGC 7145	E0	E0	11.98	40	0.05	-0.1	36.9	-20.85	21.91	FIH	FIH	26	128
NGC 7507	E0	E0	11.15	32	0.04	-0.3	35.0	-21.57	20.63	FIH	FIH	m37	215
NGC 7619	E2/E1	E3	12.00	37	0.24	0.4	71.6	-22.28	21.53	FIH	FIH/JS	64	270
NGC 7626	E1P/E2P	E1	11.99	40	0.13		71.6	-22.29	21.87	PD	JS	m19	241
IC 0179			13.40	21	0.17		94.7	-21.48		Dj	JS	122	188
IC 1459	E3	E4	10.88	45	0.26	0.5	44.5	-22.36	20.81	FIH	FIH	23	304
IC 4296	E0	E0	11.29	60	0.10		75.3	-23.10	22.07	Je	FIH	39	298

Notes. Columns (2) and (3) give the galaxy classification from the RC2 and the RSA. Column (4) gives the total apparent magnitude B_T from Burstein *et al.* (1987), except for IC 179 which is taken from the UGC. Column (6) gives the mean ellipticity between 10 and 30 arcsec. Column (5) lists the major axis effective radius r_e, calculated from the values in Burstein *et al.* (1987) and the ellipticities in column (6) (except for NGC 5846, for which r_e is taken from the RC2, and for IC 179 for which r_e is determined by fitting a de Vaucouleurs law). Column (7) gives the c_4 coefficient (in per cent) measuring the deviations of the isophotes from ellipses. The definitions and values of Bender *et al.* (1989) are used, but their a_4/a values are transformed to unit-circle deviations. If no a_4/a value is available from Bender *et al.* (1989), the source mentioned in column (11) is used. Column (8) gives the distance in Mpc, as calculated from the data listed in Faber *et al.* (1989), using an asymptotic value of the Hubble constant $H_0 = 50$ km s^{-1} Mpc^{-1}. These distances are calculated using the $D_n - \sigma$ relation. Column (9) gives the absolute magnitude M_B calculated from B_T and the distance D. Column (10) gives the mean blue surface brightness within r_e in mag arcsec^{-2}, as listed in Faber *et al.* (1989). Column (11) gives the source of the surface photometry used; Dj, Je, FIH or PDIDC. Dj gives no cos 4θ coefficients. For NGC 777 and NGC 4494 the cos 4θ coefficients from Bender *et al.* (1988) are adopted. For NGC 2749, NGC 5198, NGC 5846 and IC 179 the cos 4θ coefficients are assumed zero. Column (12) gives the source of the kinematical data used; DB, JS, FIH or BDI (Paper I). Column (13) is the major axis rotation in km s^{-1}, calculated by fitting an appropriate function to the major axis rotation data, as taken from the source(s) mentioned in (12). If no value is available from the source in (12), the unweighted mean of the datapoints beyond 10 arcsec is given. This is also done for NGC 4486. If the minor axis rotation exceeds the major axis rotation, then the minor axis rotation velocity is given. These cases are indicated by the letter m. Column (14) is the unweighted mean of the major and minor axis dispersion data points within $r_e/2$.

models affects the mass-to-light ratio that is required to fit a fixed set of observations. This effect introduces a ~5 per cent uncertainty in the mass-to-light ratios predicted by the model (depending slightly on R_Σ).

4 RESULTS

Models were constructed for all the galaxies in the sample, for both $i = 90°$ and $i = 60°$. The kinematical data and the

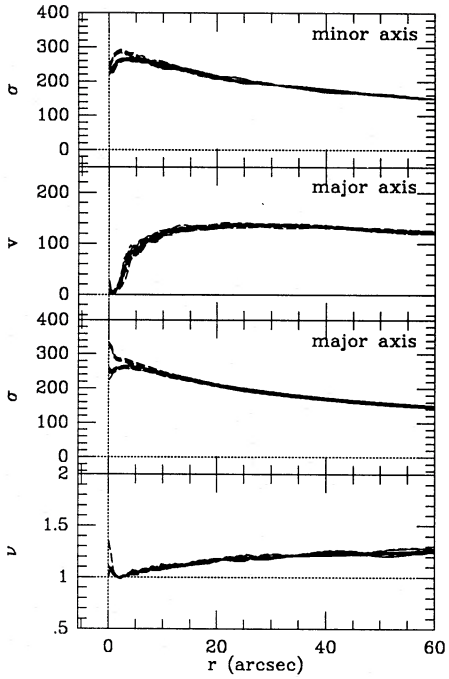

Figure 2. The kinematical predictions of an edge-on oblate model applied to pseudo surface photometry (following a Hernquist model), to which Gaussian noise was added with standard deviations $\sigma_\Sigma = 0.03$ mag, $\sigma_\varepsilon = 0.01$ and $\sigma_{c4} = 0.002$. These errors are typical for the surface photometry used here (see e.g. FIHb). Fifteen sets of pseudo surface photometry were created with different realizations of the noise. Inner cutoff radii $R_\Sigma = 3$ arcsec and $R_\varepsilon = 6$ arcsec were applied. Five curves were extrapolated inwards from R_Σ with a modified Hubble model, five with a Hernquist model and five with a Jaffe model. Top panel: minor axis dispersion; second panel: major axis rotation; third panel: major axis dispersion; bottom panel: $\nu(r)$. Beyond 4 arcsec the curves agree well.

predictions of the models for several selected galaxies are plotted in Appendix B.

In the oblate models the mass-to-light ratio Υ is chosen to optimize the fit to the minor axis dispersion profile. The following approach is adopted. First some fiducial value $\tilde{\Upsilon}$ for the mass-to-light ratio is chosen, and the predictions $\tilde{\sigma}(r)$ for the minor axis dispersion are calculated. Then for all the minor axis dispersion measurements $\sigma(r_i)$, the ratio $\theta_i \equiv \sigma(r_i)/\tilde{\sigma}(r_i)$ and its error $\Delta\theta_i = \Delta\sigma(r_i)/\tilde{\sigma}(r_i)$ are calculated. From these values the weighted mean $\bar{\theta}$ of all the θ_i with $r_i > 4$ arcsec, and its formal error $\Delta\bar{\theta}$ are calculated. The best fit for Υ is then $\Upsilon = \bar{\theta}^2 \tilde{\Upsilon}$ with formal relative error $\Delta\Upsilon/\Upsilon = 2\Delta\bar{\theta}/\bar{\theta}$. In the prolate models Υ is chosen in a similar fashion to optimize the fit to $(v_{\rm rot}^2 + \sigma^2)_{\rm min}$. The parameter k is chosen to optimize the fit to the major axis rotation data beyond 4 arcsec. This is done by first calculating the predicted major axis rotation for the fiducial value $\tilde{k} = 1$, and then calculating the weighted mean (and formal error Δk) of the ratio of the observed and predicted major axis rotation beyond 4 arcsec.

Listed in Table 2 are the parameters k and Υ, and their formal errors Δk and $\Delta\Upsilon$.‖ The mass-to-light ratios correspond to the Johnson R-band, and are calculated for the distances listed in Table 1, that were calculated from the $D_n - \sigma$ relation, assuming $H_0 = 50$ km s^{-1} Mpc^{-1}. The mass-to-light ratio derived by the model is the *only* aspect of the model that depends on the assumed distance. The mass-to-light ratios can be corrected for velocity dispersion anisotropy ($\sigma_r \neq \sigma_\theta$) as will be described in Section 4.3, which yields improved estimates $\Upsilon_R^{\rm imp}$ for the mass-to-light ratios; these are listed in column (18). Also listed in Table 2 are the type of extrapolation used inside R_Σ, and the rms error $\Delta\mu$ between the observed surface brightnesses and the surface brightnesses of the adopted model (i.e. after four Lucy iterations).

4.1 Comparison to tensor virial theorem predictions

The tensor virial theorem is formally equivalent to the density-weighted global average of the Jeans equations. It can be used to study the dynamical structure of elliptical galaxies on the basis of their global properties. It is interesting to see how results obtained from the tensor virial theorem compare to the results of the detailed models presented here.

The parameter k is in every point in the meridional plane equal to the ratio of the streaming velocity to the isotropic streaming velocity. It is thus similar to the parameter $(v/\sigma)^*$ (e.g. Davies *et al.* 1983) that describes this same quantity in terms of observable global properties. Table 2 gives $(v/\sigma)^*$ for the galaxies in the sample. Fig. 3(a) shows that there is indeed a good correlation between k and $(v/\sigma)^*$ for the galaxies in the sample.

Bacon, Monnet & Simien (1985) derive from the tensor

‖ Some of the galaxies in the sample were already studied in Paper I or II. The values of k and Υ_R listed here are not necessarily the same as those listed in Paper I or II, for two reasons: (i) in Paper I and II k and Υ were fitted by eye; and (ii) the distances used here are not the same as those used in Paper I and II.

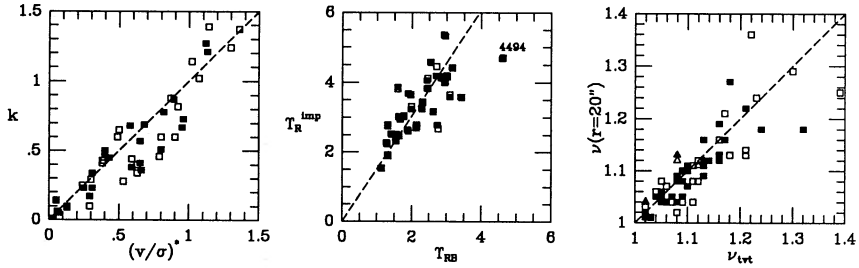

Figure 3. Comparisons of quantities derived from our models (plotted on the vertical axis) to quantities derived from the tensor virial theorem (plotted on the horizontal axis), as explained in the text. Solid symbols: $i = 90°$; open symbols: $i = 60°$. Squares: oblate models; triangles: prolate models (only in c). (a) k versus $(v/\sigma)^*$. (b) $\Upsilon_R^{\rm imp}$ (as defined by equation 13) versus Υ_{RB}. The position of NGC 4494 in this plot will be discussed in Section 4.3. (c) ν at 20 arcsec as predicted by our model versus ν_{tvt} as derived from equation (9) with $B = 0$ and $s = 3$.

Table 2. Parameters of best-fitting models.

			inclination 90°							inclination 60°							
Galaxy	Ex	S	$\Delta\mu$	k	Δk	Υ_R	$\Delta\Upsilon_R$	$(v/\sigma)^*\Upsilon_{RB}$		$\Delta\mu$	k	Δk	Υ_R	$\Delta\Upsilon_R$	$(v/\sigma)^*\Upsilon_{RB}$		Υ_R^{imp}
(1)	(2)	(3)	(4)	(5)	(6)	(7)	(8)	(9)	(10)	(11)	(12)	(13)	(14)	(15)	(16)	(17)	(18)
NGC 0636	Jf	O	1.6	1.27	0.06	2.49	0.10	1.12	2.13	1.7	1.02	0.05	2.50	0.11	1.07	2.15	2.78
NGC 0720	Hb	O	2.0	0.23	0.02	4.49	0.12	0.31	1.89								3.68
NGC 0777	Hq	O	1.9	0.34	0.04	3.82	0.11	0.31	3.00	1.8	0.29	0.03	3.87	0.11	0.30	3.02	4.18
NGC 1052	Jf	O	2.1	0.68	0.01	3.01	0.06	0.58	1.62	3.2	0.65	0.01	3.14	0.06	0.50	1.62	3.01
NGC 1379	Jf	O	1.7	1.80	0.16	1.68	0.10	1.14	1.12	1.6	1.39	0.09	1.68	0.10	1.14	1.13	1.53
NGC 1395	Jf	O	1.5	0.67	0.02	2.77	0.06	0.95	1.87	1.6	0.60	0.02	2.80	0.06	0.90	1.89	2.63
NGC 1399	Hq	O	1.6	0.23	0.02	3.79	0.09	0.25	2.44	1.8	0.25	0.03	3.79	0.09	0.24	2.46	3.83
NGC 1404	Hq	O	1.8	0.73	0.02	2.99	0.07	0.96	1.76	2.6	0.82	0.02	2.99	0.07	0.92	1.78	3.03
NGC 1407	Hq	O	1.5	0.51	0.06	4.21	0.11	0.80	2.85	1.5	0.46	0.06	4.20	0.11	0.79	2.86	4.16
NGC 1439	Jf	O	1.5			2.19	0.14		1.54	1.6			2.20	0.14		1.55	2.35
NGC 1549	Jf	O	1.8	0.41	0.02	2.58	0.06	0.65	1.40	2.0	0.40	0.02	2.60	0.06	0.63	1.41	2.53
NGC 1600	Hq	O	1.6	0.01	0.02	5.36	0.21	0.01	2.96	2.0	0.00	0.02	5.67	0.22	0.01	2.93	5.33
NGC 1700	Jf	O	1.8	0.38	0.02	2.80	0.09	0.59	1.31	3.6	0.28	0.01	3.12	0.09	0.53	1.31	2.78
NGC 2749	Hb	O	1.8			3.52	0.24		3.41	2.2			3.65	0.25		3.43	3.59
NGC 2749	Hb	P	2.9			3.85	0.29			2.3			3.59	0.27			3.59
NGC 3091	Hq	O	1.9	0.57	0.08	4.19	0.38	0.65	2.70	3.3	0.44	0.06	4.45	0.40	0.59	2.71	4.32
NGC 3379	Jf	O	1.7	0.78	0.02	2.01	0.03	0.82	1.31	1.9	0.60	0.01	2.01	0.03	0.80	1.32	1.91
NGC 3557	Jf	O	2.0	1.21	0.05	3.29	0.19	1.13	2.30	2.6	1.14	0.05	3.33	0.19	1.02	2.31	3.45
NGC 3608	Jf	O	1.6			2.23	0.08		1.27	1.7			2.26	0.08		1.28	2.26
NGC 4261	Jf	O	1.6			4.22	0.08		2.94	1.9			4.34	0.08		2.96	4.00
NGC 4261	Jf	P	1.8			4.65	0.09			1.8			4.36	0.09			4.08
NGC 4374	Hq	O	1.5	0.05	0.02	4.18	0.11	0.07	2.44	1.7	0.06	0.02	4.21	0.11	0.06	2.46	4.09
NGC 4406	Jf	O	1.7			3.11	0.10		1.66	3.6			3.22	0.10		1.67	2.97
NGC 4406	Jf	P	2.1			2.67	0.10			2.3			2.63	0.10			2.49
NGC 4472	Hq	O	1.5	0.36	0.01	3.44	0.07	0.66	1.98	1.6	0.34	0.01	3.48	0.07	0.63	1.99	3.28
NGC 4486	Hb	O	1.6	0.10	0.02	4.40	0.05	0.13	2.53	1.6	0.09	0.02	4.43	0.05	0.13	2.54	4.58
NGC 4494	Jf	O	2.5			5.01	0.17		4.60	2.6			5.08	0.17		4.62	4.69
NGC 4636	Hq	O	2.0	0.17	0.03	3.89	0.16	0.29	1.60	2.8	0.10	0.02	3.89	0.16	0.29	1.60	3.83
NGC 4649	Hq	O	1.6	0.50	0.06	3.41	0.09	0.40	2.28	2.0	0.41	0.05	3.45	0.09	0.38	2.29	3.27
NGC 4697	Hq	O	1.6	0.69	0.01	4.43	0.11	0.68	2.95	3.2	0.60	0.01	4.96	0.12	0.49	2.84	4.10
NGC 5198	Jf	O	2.0	0.14	0.05	3.30	0.15	0.05	1.77	2.4	0.14	0.05	3.31	0.15	0.05	1.78	3.03
NGC 5846	Hq	O	3.0	0.00	0.07	4.61	0.15	0.03	3.16	2.3	0.01	0.06	4.63	0.15	0.03	3.17	4.42
NGC 7144	Jf	O	1.6	1.79	0.13	2.32	0.10	1.31	1.62	1.5	1.24	0.08	2.32	0.10	1.30	1.63	2.48
NGC 7145	Hq	O	1.5	0.87	0.10	2.76	0.16	0.89	1.54	1.6	0.88	0.09	2.76	0.16	0.88	1.55	2.51
NGC 7507	Jf	O	1.6			2.36	0.06		1.55	1.6			2.36	0.06		1.55	2.32
NGC 7507	Jf	P	1.6			2.46	0.07			1.6			2.39	0.06			2.39
NGC 7619	Jf	O	1.5	0.45	0.02	3.98	0.10	0.43	3.09	2.0	0.43	0.01	4.12	0.10	0.39	3.10	3.62
NGC 7626	Jf	O	1.5			3.59	0.08		1.96	1.5			3.61	0.08		1.97	3.65
NGC 7626	Jf	P	1.5			3.48	0.08			1.5			3.41	0.08			3.43
IC 0179	Jf	O	1.9	1.87	0.05	2.56	0.09	1.45	2.74	4.9	1.37	0.03	2.57	0.09	1.36	2.76	2.73
IC 1459	Jf	O	1.5			2.61	0.10		2.12	1.7			2.77	0.11		2.12	2.70
IC 4296	Jf	O	1.5	0.48	0.10	3.17	0.29	0.40	2.61	1.5	0.43	0.09	3.17	0.29	0.38	2.62	3.17

Notes. Column (2) is the type of model used to extrapolate the observed surface brightnesses inward from R_Σ; Hb (modified Hubble profile), Hq (Hernquist model) or Jf (Jaffe model). Column (3) is the shape of the model used; O (oblate) or P (prolate). Columns (4) to (10) give the results for $i=90°$. Columns (11) to (17) give the results for $i=60°$. For NGC 720 no $i=60°$ model is constructed, since it would correspond to an unrealistically flat system. However, $i=65°$ models for this galaxy were discussed in Paper I. Columns (4/11) give the rms error $\mu_{obs}-\mu_{model}$ after four Lucy iterations, in units of 0.01 mag. Columns (5/12) and (6/13) give the best-fitting value for k and its formal error Δk. Note that k [and $(v/\sigma)^*$ in columns (9/16)] are not calculated for galaxies with either a peculiar rotation curve or $v_{min}>v_{maj}$. Column (7/14) and (8/15) give the best-fitting value for the mass-to-light ratio Υ_R in the Johnson R-band and its formal error $\Delta\Upsilon_R$. Column (9/16) is the parameter $(v/\sigma)^*$, derived from ε, v_{rot} and $\bar{\sigma}$ in Table 1, as in Davies *et al.* (1983). Column (10/17) is the mass-to-light ratio Υ_{RB} in the Johnson R-band, derived from equation (11) and the values in Table 1, as described in the text. Column (18) gives an improved estimate of the mass-to-light ratio according to equation (13). Listed is $\frac{1}{2}[\Upsilon_R^{imp}(i=90°)+\Upsilon_R^{imp}(i=60°)]$.

virial theorem that the mass-to-light ratio of an oblate elliptical galaxy with a de Vaucouleurs light profile is

$$\Upsilon=(\langle s^2\rangle/I_e r_e)h(q_a, q_t), \tag{11}$$

where h is a known function of the true and the apparent axial ratio of the galaxy, and $\langle s^2\rangle$ is the luminosity-weighted mean of the projected 'kinetic energy' $s^2=\sigma^2+\bar{v}^2$ over the entire galaxy. Table 2 gives Υ_{RB} ('R' for Johnson R-band, 'B' for Bacon) for the galaxies in the sample. Instead of $\langle s^2\rangle$, which is not accessible to the observer, $\tilde{s}^2\equiv\bar{\sigma}^2+v_{rot}^2$ is used, where $\bar{\sigma}$ and v_{rot} are as given in Table 1. Fig. 3(b) plots the relation between the mass-to-light ratios Υ_R^{imp} of our models and the Υ_{RB}. As expected there is a good correlation. The slope of the correlation is a measure of the value of $\tilde{s}^2/\langle s^2\rangle$ for our models.★★

★★ Bacon *et al.* (1985) estimated $\tilde{s}^2/\langle s^2\rangle$, and modified their mass-to-light ratios accordingly.

In Section 2.1 the tensor virial theorem was used to find an estimate $v_{tvt}(q_a, i, B)$ of the function $v(r)$. The estimates for $B=0$ can be compared to the predictions of the models at some fiducial distance $\tilde{r}$, e.g. $\tilde{r}=20$ arcsec. The result is plotted in Fig. 3(c), and shows a good correlation. The estimate v_{tvt} thus provides a useful tool in understanding the function $v(r)$, in spite of the simplicity of the assumptions that it is based on.

4.2 Do elliptical galaxies have $\sigma_r = \sigma_\theta$?

To characterize the ratio of the predicted $v(r)$ to the observations v_i (being the observed v at radius r_i) for the galaxies in the sample, the following approach is adopted. For every datapoint v_i the ratio $\mathscr{R}_i = v(r_i)/v_i$ with formal relative error $\Delta\mathscr{R}_i/\mathscr{R}_i = \Delta v_i/v_i$ is calculated. Then the weighted mean $\bar{\mathscr{R}}$ of the $\mathscr{R}_i$ with $r_i > 4$ arcsec is calculated, together with its formal error $\Delta\bar{\mathscr{R}}$. The results are listed in Table 3, and plotted as a function of ellipticity in Fig. 4. A value $\bar{\mathscr{R}} > 1$ indicates that the model predicts too much motion on the major axis, and thus that the distribution function must depend on a third integral.

In Fig. 4 the sample has been divided into several groups. Five galaxies in the sample have $k > 1$ [i.e. $(v/\sigma)^* > 1$]. These galaxies are plotted as starred symbols in Fig. 4 (see also Appendix B, Fig. 7c). Two of these galaxies (NGC 1379 and NGC 7144) have very low ellipticity ($\varepsilon = 0.03$), a large isophote twist ($\gtrsim 20°$) and low rotation velocity ($v_{rot} \approx 30$ km s^{-1}

Table 3. Comparison of predictions and observations.

		inclination 90°								inclination 60°							
Galaxy	S	$\bar{\mathscr{R}}$	$\Delta\bar{\mathscr{R}}$	$\bar{\mathscr{R}}^+$	$\Delta\bar{\mathscr{R}}^+$	$\bar{\Sigma}$ minor	$\Delta\bar{\Sigma}$	$\bar{\Sigma}$ major	$\Delta\bar{\Sigma}$	$\bar{\mathscr{R}}$	$\Delta\bar{\mathscr{R}}$	$\bar{\mathscr{R}}^+$	$\Delta\bar{\mathscr{R}}^+$	$\bar{\Sigma}$ minor	$\Delta\bar{\Sigma}$	$\bar{\Sigma}$ major	$\Delta\bar{\Sigma}$
(1)	(2)	(3)	(4)	(5)	(6)	(7)	(8)	(9)	(10)	(11)	(12)	(13)	(14)	(15)	(16)	(17)	(18)
NGC 0636	O	0.89	0.05	0.89	0.05	1.10	0.11	1.28	0.13	0.91	0.05	0.91	0.05	1.11	0.11	1.31	0.14
NGC 0720	O	1.22	0.04	1.29	0.06			0.98	0.08								
NGC 0777	O	0.91	0.03	0.93	0.04	1.09	0.06	1.12	0.11	0.93	0.03	0.95	0.04	1.10	0.06	1.13	0.11
NGC 1052	O	1.00	0.02	1.01	0.02	1.15	0.04	1.09	0.03	1.04	0.02	1.05	0.02	1.18	0.04	1.11	0.03
NGC 1379	O	1.09	0.07	1.13	0.15			1.03	0.19	1.10	0.07	1.14	0.15			1.02	0.19
NGC 1395	O	1.05	0.03	0.96	0.04					1.07	0.03	0.97	0.04				
NGC 1399	O	0.99	0.02	1.02	0.04	1.09	0.07	1.21	0.12	0.99	0.02	1.01	0.04	1.10	0.07	1.23	0.12
NGC 1404	O	0.99	0.02	0.98	0.03	1.17	0.09	1.09	0.06	0.98	0.02	0.96	0.03	1.18	0.09	1.13	0.06
NGC 1407	O	1.01	0.03	0.97	0.12					1.01	0.03	0.97	0.12				
NGC 1439	O	0.93	0.07							0.94	0.07						
NGC 1549	O	1.02	0.03	1.03	0.05	0.92	0.07	1.23	0.09	1.03	0.03	1.03	0.05	0.93	0.07	1.24	0.09
NGC 1600	O	1.01	0.04	1.09	0.10					1.06	0.04	1.16	0.10				
NGC 1700	O	1.00	0.04	1.00	0.04	1.01	0.04	1.05	0.06	1.11	0.04	1.11	0.04	1.03	0.04	1.05	0.06
NGC 2749	O	0.98	0.07	1.01	0.09	1.89	0.32	1.26	0.27	1.02	0.07	1.06	0.10	1.91	0.32	1.26	0.27
NGC 2749	P	1.05	0.07	1.09	0.10	2.38	0.40	1.39	0.29	1.02	0.07	1.06	0.10	2.37	0.40	1.38	0.29
NGC 3091	O																
NGC 3379	O	1.04	0.02	1.09	0.03	1.09	0.06	1.20	0.05	1.06	0.02	1.11	0.03	1.10	0.06	1.21	0.05
NGC 3557	O	0.95	0.06	0.90	0.12					0.97	0.06	0.91	0.12				
NGC 3608	O	0.98	0.03	0.97	0.04			1.11	0.09	1.01	0.03	0.99	0.04			1.13	0.09
NGC 4261	O	1.06	0.02	1.09	0.03	1.08	0.03	0.96	0.04	1.08	0.02	1.11	0.03	1.09	0.03	0.96	0.04
NGC 4261	P	1.12	0.02	1.14	0.03	1.14	0.04	0.99	0.04	1.09	0.02	1.12	0.03	1.15	0.04	0.99	0.04
NGC 4374	O	1.03	0.03	1.03	0.04			1.20	0.08	1.02	0.03	1.02	0.04			1.20	0.08
NGC 4406	O	1.04	0.03							1.09	0.04						
NGC 4406	P	1.06	0.04							1.05	0.03						
NGC 4472	O	1.06	0.02	1.09	0.05					1.07	0.02	1.11	0.05				
NGC 4486	O	0.96	0.01	0.94	0.02					0.97	0.01	0.96	0.02				
NGC 4494	O	1.07	0.03	1.08	0.04	1.18	0.09	1.20	0.09	1.08	0.03	1.09	0.04	1.19	0.09	1.22	0.09
NGC 4636	O	1.01	0.04	1.05	0.11					1.02	0.04	1.08	0.11				
NGC 4649	O	1.04	0.04							1.06	0.04						
NGC 4697	O	1.09	0.03	1.16	0.05			1.00	0.10	1.20	0.03	1.32	0.06			1.00	0.10
NGC 5198	O	1.09	0.06	1.12	0.08	1.09	0.12	1.01	0.12	1.09	0.06	1.12	0.08	1.09	0.12	1.03	0.12
NGC 5846	O	1.04	0.04							1.05	0.04						
NGC 7144	O	0.93	0.05	0.93	0.09			1.22	0.14	0.94	0.05	0.93	0.10			1.22	0.14
NGC 7145	O	1.10	0.06	1.11	0.16					1.10	0.06	1.11	0.16				
NGC 7507	O	1.00	0.03	0.98	0.04	1.00	0.07	1.05	0.08	1.00	0.03	0.99	0.04	1.00	0.07	1.06	0.08
NGC 7507	P	1.02	0.03	1.00	0.04	1.02	0.07	1.06	0.08	1.01	0.03	0.97	0.04	1.03	0.07	1.06	0.09
NGC 7619	O	1.11	0.03	1.17	0.05	1.38	0.12	0.91	0.24	1.13	0.03	1.18	0.05	1.39	0.12	0.92	0.24
NGC 7626	O	0.98	0.03	0.97	0.05	1.00	0.10	0.83	0.14	0.99	0.03	0.98	0.05	1.00	0.10	0.84	0.15
NGC 7626	P	1.01	0.03	0.99	0.05	1.10	0.12	0.89	0.15	1.00	0.03	0.98	0.05	1.09	0.12	0.88	0.15
IC 0179	O	0.92	0.05	0.92	0.05	1.38	0.10	1.14	0.14	0.96	0.05	0.96	0.05	1.40	0.10	1.13	0.14
IC 1459	O	0.97	0.03	0.97	0.05			1.01	0.07	1.02	0.03	1.03	0.06			1.00	0.07
IC 4296	O																

Notes. Column (2) is the shape of the model used; O (oblate) or P (prolate). Columns (3) to (10) list the results for $i = 90°$, and columns (11–18) for $i = 60°$. Values are only listed if they are based on data for at least two different radii (for HGC 3091 and NGC 4296 this results in no values being listed). Columns (3/11) and (4/12) list the value of $\bar{\mathscr{R}}$ (defined in the text) and its formal error. A value $\bar{\mathscr{R}} > 1$ indicates that $\sigma_r > \sigma_\theta$, and thus that the distribution function must depend on a third integral. Columns (5/13) and (6/14) list the value of $\bar{\mathscr{R}}^+$ together with its formal error. The quantity $\bar{\mathscr{R}}^+$, is similar to the quantity $\bar{\mathscr{R}}$, but only datapoints with $r > 0.2 r_e$ are taken into account. Column (7/15) and (8/16) list the value of $\bar{\Sigma}$ (defined in the text) on the minor axis, and its formal error. Column (9/17) and (10/18) list the value of $\bar{\Sigma}$ on the major axis, and its formal error. A value $\bar{\Sigma} > 1$ indicates that the mass-to-light ratio rises with radius.

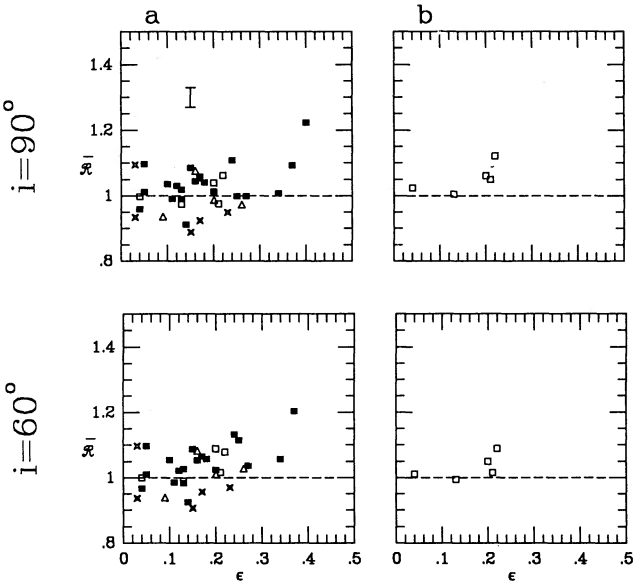

Figure 4. Plotted is the ratio $\bar{\mathscr{R}}$ as a function of ellipticity. A value $\bar{\mathscr{R}} > 1$ indicates that the model predicts too much motion on the major axis, and thus that the galaxy must have $\sigma_r > \sigma_\theta$. The median error in $\bar{\mathscr{R}}$ is shown in the upper left panel. Upper panels: $i = 90°$; lower panels: $i = 60°$. (a) Oblate models, (b) prolate models. Symbols: solid squares: galaxies with $v_{maj} > v_{min}$; open triangles: galaxies with $v_{maj} > v_{min}$ and a peculiar rotation curve; starred symbols: galaxies with $v_{maj} > v_{min}$ and $k > 1$; open squares: galaxies with $v_{min} > v_{maj}$.

and $v_{rot}/\sigma \approx 0.2$). These galaxies have $k > 1$ because the models for these galaxies are nearly spherical, and thus have little azimuthal motion. It is likely that these galaxies are viewed at a special viewing angle, such that they appear rather round, whereas intrinsically they are not necessarily close to spherical at all. The other three galaxies in the sample with $k > 1$ (NGC 636, NGC 3557, IC 179) are of a different nature. They have normal ellipticity ($\varepsilon \approx 0.2$), but an uncommonly large rotation velocity ($v_{rot}/\sigma \approx 0.6$). Their large rotation velocity causes $\bar{\mathscr{R}}$ to be well below unity. In IC 179 one has to choose k so large to fit the observed rotation curve, that the predicted major axis dispersion drops below zero (see Fig. 7c). It is likely that these galaxies contain a disc component, and are misclassified S0s. NGC 636 has discy isophotes, supporting this idea. The value of $\bar{\mathscr{R}}$ for these galaxies thus gives no information on the anisotropy of their velocity dispersion tensor. In the remainder of this subsection, NGC 636, NGC 3557 and IC 179 are excluded from the discussion.

For the five galaxies in the sample with $v_{min} > v_{maj}$ (plotted as open squares in Fig. 4) both oblate and prolate models are constructed (see also Appendix B, Fig. 7e). The prolate models, especially for the flatter galaxies, tend to have $\bar{\mathscr{R}} > 1$, and thus predict too much motion on the major axis. This discrepancy can be reduced by turning the models more end-on, *cf.* Fig. 1b. However, they are then intrinsically rather elongated, which is physically not very plausible, as well as it is statistically not very plausible that a majority of prolate galaxies is viewed close to end-on. If the galaxies with $v_{min} > v_{maj}$ are indeed close to prolate, it is thus more likely that they are viewed near to broadside-on, and possess some radial anisotropy. The oblate models for these galaxies follow the trend of the oblate models for the other galaxies.

The galaxies in the sample that have a peculiar rotation curve (NGC 1439, NGC 3608, NGC 4494 and IC 1459, which are plotted as open triangles in Fig. 4, as well as NGC 4406 and NGC 7626 which are plotted as open squares) do not seem to occupy any particular place in the diagram of $\bar{\mathscr{R}}$ versus ε. From this and the fits presented in Appendix B (Fig. 7d,e), it is concluded that there is no evidence for peculiar behaviour in the even part of the distribution functions of these galaxies (which is probed by $v_{rot}^2 + \sigma^2$; the odd part is probed by v_{rot}), except for the case of NGC 4494 which has a peculiar central dip in the quantity $v_{rot}^2 + \sigma^2$ (see also Section 4.3).

The remaining 23 galaxies in the sample have $v_{maj} > v_{min}$, $k < 1$ and no peculiar rotation curve (see also Appendix B, Fig. 7a,b). These galaxies are plotted as solid squares in Fig. 4. Of these 23 galaxies, 18 galaxies (~ 50 per cent of the total sample) have no detectable minor axis rotation beyond the 3σ level. Especially for these galaxies, oblate models are likely to be a very useful approximation.

The average of $\bar{\mathscr{R}}$ for all oblate models (excluding NGC 636, NGC 3557 and IC 179) is $\langle \bar{\mathscr{R}} \rangle = 1.016 \pm 0.005$ for $i = 90°$ and $\langle \bar{\mathscr{R}} \rangle = 1.029 \pm 0.005$ for $i = 60°$. As expected from Fig. 1(a), this average rises with decreasing inclination. Note that the average inclination angle for a randomly oriented sample is 61°.35. It is concluded ($> 3\sigma$ result) that the models on average predict too much motion on the major axis, and thus that elliptical galaxies as a class have $\sigma_r > \sigma_\theta$.

Recently it has been argued that a substantial fraction of elliptical galaxies has a disc component (e.g. Scorza & Bender 1990; Rix & White 1990). If so, elliptical galaxies are even more radially anisotropic, since the presence of a disc decreases $\bar{\mathscr{R}}$, as was argued for in the case of NGC 636, NGC 3557 and IC 179.

There seems to be a trend in Fig. 4 for $\bar{\mathscr{R}}$ to increase with ε. One can try to understand this trend by studying the ratio

$$\mathscr{R}_{tvt}(q_a, i, B) \equiv v_{tvt}(q_a, i, B = 0)/v_{tvt}(q_a, i, B). \qquad (12)$$

Because of continuity $\nu(r) \to 1$ for $r \to 0$. Discrepancies between the models and the observations are thus likely to be more pronounced in the outer parts of the galaxies in the sample. Therefore a quantity $\bar{\mathscr{R}}^+$, that is defined as $\bar{\mathscr{R}}$ but does not take datapoints with $r < 0.2 r_e$ into account, is also calculated for all the galaxies in the sample. The values of $\bar{\mathscr{R}}^+$ and their formal errors are listed in Table 3. As expected $\bar{\mathscr{R}}^+ > \bar{\mathscr{R}}$ on average, but the statistics on $\bar{\mathscr{R}}^+$ are poorer since $\bar{\mathscr{R}}^+$ is calculated from fewer datapoints. Fig. 5(a) plots $\bar{\mathscr{R}}^+$ for the oblate models, together with curves of $\mathscr{R}_{tvt}(B = cst)$. The trend in the data is well explained by these curves. In Fig. 5(b) similar curves are plotted for the prolate models.

It is straightforward to construct a similar argument as in Section 2.1 for galaxies in which the velocity ellipsoid aligns with cylindrical coordinate axes everywhere, i.e. $\overline{v_R v_z} = 0$. Even though this case seems less likely than the case of alignment with spherical coordinate axes ($\overline{v_r v_\theta} = 0$), it cannot be excluded. In Fig. 5(c) $\mathscr{R}_{tvt}$ is plotted for models that have $\sigma_R^2 = \overline{v_\phi^2}$ everywhere. Van der Marel & Cinzano (1991) solved the Jeans equations for NGC 720 under this constraint, and obtained a good fit for $i = 90°$, consistent with Fig. 5c.

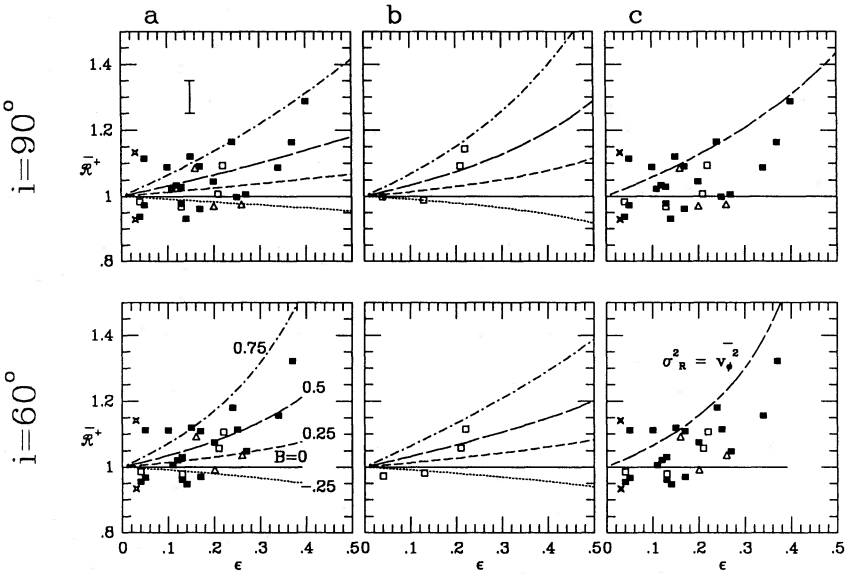

Figure 5. The data for $\bar{\mathscr{R}}^+$ are modelled with $\mathscr{R}_{tvt}$ (as calculated with $s=3$ in equation 5). The median error in $\bar{\mathscr{R}}^+$ is shown in the upper left panel. Symbols are as in Fig. 4. Note that $\bar{\mathscr{R}}^+$ cannot be calculated for galaxies for which insufficient data are available beyond $0.2r_e$. Therefore, not all the galaxies in the sample appear in these plots. NGC 636, NGC 3557 and IC 179 are omitted for reasons explained in the text. Upper panels: $i=90°$, lower panels: $i=60°$. (a) Oblate models and alignment with spherical coordinate axes, i.e. $\overline{v_r v_\theta}=0$. Plotted is $\mathscr{R}_{tvt}$ for $B=-0.25$ (dotted), $B=0$ (solid), $B=0.25$ (short dashed), $B=0.50$ (long dashed) and $B=0.75$ (short dash-dot). (b) Idem for prolate models. (c) Oblate models and alignment with cylindrical coordinate axes, i.e. $\overline{v_R v_z}=0$. Plotted is $\mathscr{R}_{tvt}$ for $\sigma_z=\sigma_R$ [i.e. $f=f(E,L_z)$; solid curve] and for $\sigma_R^2=\overline{v_\phi^2}$ (long-short dash).

4.3 Mass-to-light ratios

The mass-to-light ratios Υ_R listed in Table 2 are obtained by optimizing the fit of the model to the minor axis data. From definitions of $\bar{\mathscr{R}}$ and v it follows that the fit to the major axis data is optimized if the mass-to-light ratio is $\Upsilon_R/\bar{\mathscr{R}}^2$. Introducing radial anisotropy into the model would redistribute motion between the major and minor axis. An improved estimate for the true mass-to-light ratio of a galaxy is therefore

$$\Upsilon_R^{imp}=[1+(1/\bar{\mathscr{R}}^2)]\Upsilon_R/2\approx\Upsilon_R/\bar{\mathscr{R}}. \quad (13)$$

For the galaxies in the sample the average of $\Upsilon_R^{imp}(i=90°)$ and $\Upsilon_R^{imp}(i=60°)$ is given in column (18) of Table 2. These values are used throughout this subsection. The difference between $\Upsilon_R^{imp}(i=90°)$ and $\Upsilon_R^{imp}(i=60°)$ is generally insignificant (~ 1 per cent). For those galaxies for which both oblate and prolate models are constructed, the mass-to-light ratio of the oblate and that of the prolate model are very similar. For this reason we restrict ourselves in this subsection to the mass-to-light ratios of the oblate models. The (unweighted) average mass-to-light ratio for the galaxies in the sample is $(M/L)_R=(3.32\pm0.14)h_{50}$ [in units of $(M/L)_\odot$]. This corresponds to a blue mass-to-light ratio $(M/L)_B=(5.93\pm0.25)h_{50}$.

The global properties of elliptical galaxies, such as luminosity L, radius r, projected velocity dispersion σ, surface brightness μ etc. are known to form a two-dimensional family: the 'fundamental plane' (FP) (Dressler *et al.* 1987; Djorgovski & Davis 1987). The FP-relation is

$$L=C\sigma^{2.65}\mu^{-0.65}, \quad (14)$$

where C is a constant. An alternative form of this equation is the so-called '$D_n-\sigma$ relation' (Dressler *et al.* 1987). The FP relation can be rewritten in terms of the radius r, using $\mu=L/r^2$. Morphological parameters describing the shape of the light distribution and the dynamical anisotropies of the stars do not correlate with the FP. Djorgovski & Davis (1987) therefore argue that elliptical galaxies form a $2+N$ parameter family. From simple physical arguments (Djorgovski *et al.* 1988) one expects for an elliptical galaxy

$$L=K^2\sigma^4\mu^{-1}(M/L)^{-2}, \quad (15)$$

where K is an ill-defined function that depends on the shape, density structure, kinematical structure, evolutionary history, etc. of the galaxy. Combination of equations (14) and (15) yields

$$(M/L)=C^{-0.75}KL^{0.25}\mu^{-0.01}. \quad (16)$$

In formulae based on the (tensor) virial theorem or core fitting, one essentially derives (M/L) by putting $K^2=cst$ in equation (15) *a priori*, and not surprisingly, a correlation of the form $(M/L)\propto L^{0.25}$ is found (Kormendy 1987; Faber *et al.* 1987). The mass-to-light ratios determined in the present paper allow a more careful treatment of this issue, for three reasons: (i) fits are made to the entire major and minor axis kinematical profiles; (ii) the influence of rotation on the total kinetic energy is not neglected; and (iii) a correction for velocity dispersion anisotropy is applied (equation 13).

The distances in Table 1 are derived from the $D_n-\sigma$ relation. The existence of this relation hinges on the existence of the relation equation (16). In examining the mass-to-light ratios derived by our models, for correlations with the FP parameters, a certain amount of circular reasoning is thus introduced. In Appendix C it is demonstrated that this artificially reduces the intrinsic scatter around equation (16) by a

factor ~ 3. The scatter due to observational errors in D_n and σ is not affected.

In Fig. 6 the mass-to-light ratios Υ_R^{imp} of the galaxies in the sample are plotted versus other global properties. Linear correlation coefficients (Pearson's r) are listed in the bottom right corner of every panel. In Fig. 6(a) $\log(\Upsilon_R^{imp})$ is plotted versus blue absolute magnitude M_B (Table 1) for the galaxies in the sample. NGC 636, NGC 4494 and NGC 4697 seem not to follow the correlation defined by the other galaxies. NGC 4494 and NGC 4697 have large residual velocities with respect to the 'Virgo infall + Great Attractor' model of Lynden-Bell *et al.* (1988) (426 and 744 km s^{-1}, respectively). This suggests that the distances towards these galaxies have been underestimated, which would increase M_B and Υ_R^{imp} with respect to their true values, consistent with Fig. 6(a). The reason for this underestimation can be understood from the fact that distances derived with the FP-relation scale as $D \propto \sigma^{(2.65/2)}$ (equation 14): NGC 4494 has a kinematically peculiar core with a central 'dip' in the velocity dispersion (Fig. 7d), whereas the central velocity dispersion for NGC 4697 reported by Faber *et al.* (1989) is lower than that reported in Paper I. The dotted lines in Fig. 6(a) show how the position of NGC 4494 changes if its distance is chosen to fit exactly the 'Virgo infall + Great Attractor' model, and how the position of NGC 4697 changes if its distance is derived from the central σ reported in Paper I. NGC 636 is the least luminous galaxy in the sample. In Section 4.2 it was argued that NGC 636 is a misclassified S0. Even though this does not explain why NGC 636 should not follow the general trend in Fig. 6a, it does make it suspicious. NGC 4494, NGC 4697 and NGC 636 are excluded from the discussion (and the calculations) in the remainder of this subsection, and are plotted as open symbols in the remaining panels of Fig. 6.

The least-squares fit to the values in Fig. 6(a) is $(M/L) \propto L^{0.35 \pm 0.05}$ (solid line). This indicates that $K \propto L^{0.10}$, *cf.* equation (16). The residuals $\delta \log(\Upsilon_R^{imp})$ with respect to this least-squares fit were found not to correlate with either $\log \sigma$, μ_e or $\log r_e$. A principal component analysis will thus show that the vector of (M/L) in the fundamental plane is approximately parallel to the vector of L. The vectors of σ, μ_e and r_e make an angle with that of L, and thus show weaker (but detectable) correlations with (M/L) (Figs 6b,c,d).

A possible second parameter determining the mass-to-light ratio of elliptical galaxies must be sought in the remaining N dimensions of the manifold of elliptical galaxies, and is due to the factor K in equation (16). Fig. 6(e) plots $\log(\Upsilon_R^{imp})$ versus ε. In Fig. 6(f) $\log(\Upsilon_R^{imp})$ is plotted versus the boxyness/discyness parameter c_4 (Table 1). Bender *et al.* (1989), using a virial theorem formula, found that the average mass-to-light ratio of the boxy galaxies in their sample was nearly twice as large as that of the discy galaxies. The mass-to-light ratios derived here incorporate the effects of rotation and velocity dispersion anisotropy and can thus shed more light on this issue. The average mass-to-light ratio for the boxy galaxies in our sample is 3.39 ± 0.21 and for the discy galaxies 3.04 ± 0.28, the difference being only marginally significant. The weak correlation between $\log(\Upsilon_R^{imp})$ and

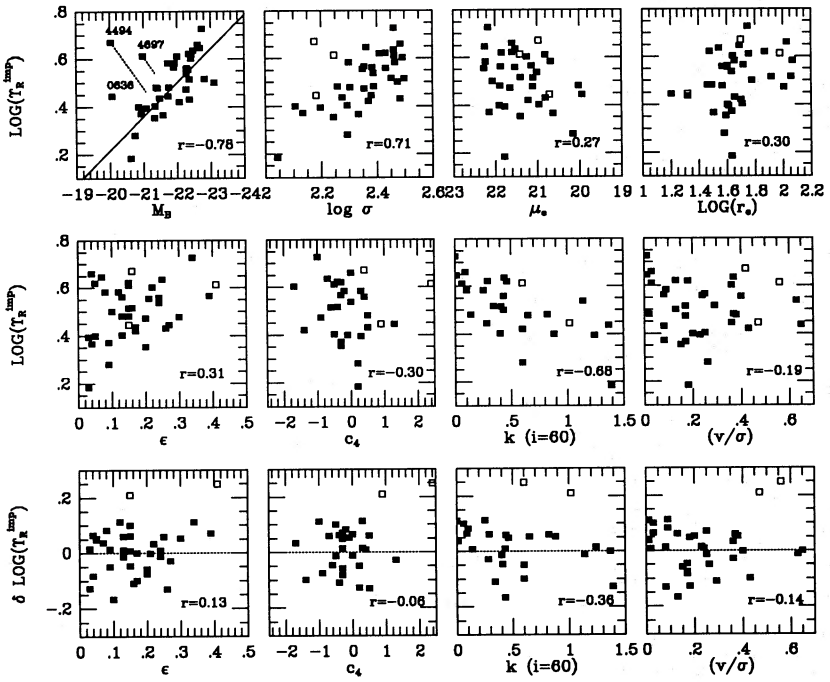

Figure 6. (a) (Upper left panel) $\log(\Upsilon_R^{imp})$ versus M_B. The line is the least-squares fit. NGC 636, NGC 4494 and NGC 4697 are excluded from the fit, for reasons explained in the text. These galaxies are plotted as open squares in the remaining panels of this figure. NGC 4494 and NGC 4697 move along the dotted lines if their assumed distances are increased as explained in the text. The number in the bottom right corner of every panel is Pearson's linear correlation coefficient (excluding NGC 636, NGC 4494 and NGC 4697). (b–d) $\text{Log}(\Upsilon_R^{imp})$ versus $\log \sigma$, μ_e and $\log r_e$, respectively. (e–h) (Middle panels) $\log(\Upsilon_R^{imp})$ versus ε, c_4, $k(i=60°)$ and (v/σ), respectively. (i–l) (Lower panels) residuals with respect to the line in (a) plotted versus ε, c_4, $k(i=60°)$ and (v/σ), respectively.

c_4 in Fig. 6(f) can be explained entirely from the fact that boxy galaxies generally have higher luminosities than discy ones (Bender *et al.* 1989), since the residuals $\delta \log(\Upsilon_R^{imp})$ do not correlate with c_4 (Fig. 6j). It is concluded that c_4 is not a second parameter determining the mass-to-light ratio of elliptical galaxies.

In Fig. 6(g) $\log(\Upsilon_R^{imp})$ is plotted versus the parameter k of our models at inclination $i=60°$. There is a clear correlation: galaxies with smaller k tend to have higher mass-to-light ratios. This correlation is partially explained by the fact (Bender *et al.* 1989) that galaxies with small k tend to be more boxy, and tend to have higher luminosities, but not entirely, since the residuals $\delta \log(\Upsilon_R^{imp})$ also correlate with $k(i=60°)$ (Fig. 6k), albeit weaker. These correlations do not change if $\log(\Upsilon_R^{imp})$ is plotted versus $k(i=90°)$ or $(v/\sigma)^*$. However, there is no significant correlation of $\log(\Upsilon_R^{imp})$ with (v/σ) (Fig. 6h,l). It is concluded that k, or equivalently $(v/\sigma)^*$, is a second parameter determining the mass-to-light ratio of elliptical galaxies.

4.4 Does the mass-to-light ratio rise with radius?

If the mass-to-light ratio of the galaxies in the sample rises with radius, one expects the ratio of the observed velocities to the predicted velocities also to rise with radius. To find out if this is indeed the case, quantities $\overline{\Sigma}_{min}$ and $\overline{\Sigma}_{maj}$ are defined, that measure this ratio on the minor and the major axis. For the oblate models, for all datapoints σ_i for the minor axis dispersion, the ratio $\Sigma_i = \sigma_i/\tilde{\sigma}(r_i)$ is calculated, where $\tilde{\sigma}(r)$ is the prediction of the model. The weighted mean $\overline{\Sigma}_<$ of all the Σ_i with $r_i < 0.6 r_e$ and the weighted mean $\overline{\Sigma}_>$ of all the Σ_i with $r_i > 0.6 r_e$ are calculated. The quantity $\overline{\Sigma}_{min}$ is then defined as $\overline{\Sigma}_{min} \equiv \overline{\Sigma}_>/\overline{\Sigma}_<$. For the prolate models $\overline{\Sigma}_{min}$ is calculated in a similar fashion, by calculating ratios of the observed to the predicted $(v_{rot}^2+\sigma^2)_{min}^{1/2}$. The quantity $\overline{\Sigma}_{maj}$ is defined by calculating ratios of the observed to the predicted $(v_{rot}^2+\sigma^2)_{maj}^{1/2}$. The values of $\overline{\Sigma}$ on the minor and the major axis for the galaxies in the sample are given in Table 3. Only for about half of the galaxies in the sample are enough data available beyond $0.6 r_e$ to calculate $\overline{\Sigma}$. There is a clear tendency for $\overline{\Sigma}$ to exceed unity, on both the major and the minor axis, for both $i=90°$ and $i=60°$. The weighted mean over all the galaxies in the sample (using both the major and the minor axis values) is $\langle\overline{\Sigma}\rangle = 1.09$ for $i=90°$ and $\langle\overline{\Sigma}\rangle = 1.10$ for $i=60°$. The formal error on these quantities is 0.01. It is concluded that the models predict velocities that are *on average* too low in the outer parts of the galaxies in the sample.

In Section 4.2 it was demonstrated that the galaxies in the sample are on average radially anisotropic, whereas the models are not. Models in which the velocity dispersion tensor is radially anisotropic have velocity dispersion profiles that fall off steeper in the outer parts than those of the models used here, because the higher radial velocities are predominantly perpendicular to the line of sight (compare with Tonry 1983 and Merritt 1985). In such models the discrepancy between observations and predictions will thus be even larger than the discrepancy observed here. It can thus be concluded that *no* axisymmetric constant mass-to-light ratio models can fit the kinematical observations in the outer parts of elliptical galaxies. This however, does not necessarily mean that dark haloes *must* be present in elliptical galaxies, since the effects of triaxiality have not been modelled.

Saglia (1990) studied models of the type introduced by Bertin & Stiavelli (1984). These models are very radially anisotropic in their outer parts. Saglia finds that the velocity dispersion profiles predicted by one-component constant mass-to-light ratio models of this type fall off too steeply in the outer parts. This is consistent with the conclusion presented here. Note however, that the velocity dispersion profiles predicted by Saglia's models will also fall off too steeply in the outer parts, if real elliptical galaxies are not as radially anisotropic as his models.

5 CONCLUSIONS

In this paper a model is used that predicts the kinematics of an elliptical galaxy on the basis of observed surface photometry. Three assumptions are made: (i) axisymmetry; (ii) constant mass-to-light ratio; and (iii) $\sigma_r = \sigma_\theta$. This model was used previously by Binney, Davies & Illingworth (1990, Paper I) and van der Marel, Binney & Davies (1990, Paper II) to model the kinematics of a few selected galaxies. In the present paper the model is applied to 37 galaxies (forming a rather inhomogeneous and incomplete sample) for which high-quality CCD surface photometry and both major and minor axis kinematical data are available in the literature. Both oblate and prolate models are constructed. By fitting the models to the kinematical profiles on both the major and the minor axis, it is possible to calculate accurate mass-to-light ratios, and assess the validity of the assumptions of the model. The following conclusions are drawn.

(i) Elliptical galaxies as a class have $\sigma_r > \sigma_\theta$ (i.e. distribution functions that depend on a third integral), even though individual galaxies can sometimes be fit rather well by models with $\sigma_r = \sigma_\theta$.

(ii) The average mass-to-light ratio for the galaxies in the sample is $(M/L)_R = (3.32 \pm 0.14) h_{50}$ [in units of $(M/L)_\odot$]. This corresponds to a blue mass-to-light ratio $(M/L)_B = (5.93 \pm 0.25) h_{50}$.

(iii) The mass-to-light ratio correlates with total luminosity according to $(M/L) \propto L^{0.35 \pm 0.05}$. The quantity $(v/\sigma)^*$ (or equivalently the parameter k of our models) is identified as a second parameter in this relation. Galaxies with high $(v/\sigma)^*$ tend to have a low mass-to-light ratio (for their luminosity).

(iv) Axisymmetric constant mass-to-light ratio models cannot fit the available kinematical data on the outer parts of elliptical galaxies, since the velocities predicted by such models fall off too steeply in the outer parts. This does not necessarily imply that dark haloes *must* be present, since the effects of triaxiality have not been modelled.

For the galaxies with a peculiar rotation curve (counter-rotating or kinematically misaligned core) no evidence is found for peculiar behaviour in the even part of their distribution functions, as probed by $(v_{rot}^2+\sigma^2)$, except possibly for NGC 4494. Conclusion (i) is consistent with N-body simulations of dissipationless collapse, in which the end product is radially anisotropic in its outer parts (van Albada 1982).

Our models have the advantage that the Jeans equations form a closed set, such that the dynamical quantities can be evaluated. A disadvantage is that the distribution function of the model [which must be of the form $f(E,L_z)$] is not speci-

fied. For models like ours $f(E,L_z)$ could in principle be recovered (e.g. Dejonghe 1986), but there is no guarantee that it is everywhere positive. To obtain models with $\sigma_r \neq \sigma_\theta$ distribution functions of the form $f(E,L_z,I_3)$ must be studied. For such distribution functions the Jeans equations are not a closed set, since only two equations constrain the four variables σ_r^2, $\overline{v_\phi^2}$, σ_θ^2 and $\overline{v_r v_\theta}$. One possible approach is then to follow Bacon (1985) by assuming $\overline{v_r v_\theta}=0$, assuming some plausible functional form for the function $\beta \equiv 1-(\sigma_\theta^2/\sigma_r^2)$, and solving the Jeans equations. Other assumptions to close the Jeans equations are also possible (Fillmore 1986). Instead of solving the Jeans equations one can also specify an explicit functional form for the distribution function, and fit the free parameters of the model to the observations, as does e.g. Saglia (1990). One step further is to allow the models to be triaxial, like those of e.g. Statler (1987). From the observational side it is important to enlarge the available sample with a number of flat (E3/E4) galaxies, since for those galaxies radial anisotropy is most easily detectable (see Fig. 5).

ACKNOWLEDGMENTS

The author thanks Tim de Zeeuw and Marijn Franx for commenting on an early version of this paper, James Binney for originating the modelling technique employed here, and for providing constructive criticism that helped improve the presentation of the paper, and Donald Lynden-Bell and Simon White for providing comments that helped improve Section 4.3.

REFERENCES

Bacon, R., 1985. *Astr. Astrophys.*, **143,** 84.
Bacon, R., Monnet, G. & Simien, F., 1985. *Astr. Astrophys.*, **152,** 315.
Bender, R., Döbereiner, S. & Möllenhof, C., 1988. *Astr. Astrophys. Suppl.*, **74,** 385.
Bender, R., Surma, P., Döbereiner, S., Möllenhof, C. & Madejsky, R., 1989. *Astr. Astrophys.*, **217,** 35.
Bertin, G. & Stiavelli, M., 1984. *Astr. Astrophys.*, **137,** 26.
Binney, J. J., 1978. *Mon. Not. R. astr. Soc.*, **183,** 501.
Binney, J. J., 1980. *Mon. Not. R. astr. Soc.*, **190,** 873.
Binney, J. J., Davies, R. L. & Illingworth, G. D., 1990. *Astrophys. J.*, **361,** 78 (Paper I).
Burstein, D., Davies, R. L., Dressler, A., Faber, S. M., Stone, R. P. S., Lynden-Bell, D., Terlevich, R. & Wegner, G., 1987. *Astrophys. J. Suppl.*, **64,** 601.
Davies, R. L. & Birkinshaw, M., 1988. *Astrophys. J. Suppl.*, **68,** 409 (DB).
Davies, R. L., Efstathiou, G., Fall, S. M., Illingworth, G. D. & Schechter, P. L., 1983. *Astrophys. J.*, **266,** 41.
Dejonghe, H., 1986. *Phys. Rept.*, **133,** 217.
de Vaucouleurs, G., de Vaucouleurs, A. & Corwin, H. G., 1976. *Second Reference Catalogue of Bright Galaxies* (RC2), University of Texas Press, Austin.
de Zeeuw, P. T., 1991. In: *Morphological and Physical Classification of Galaxies,* eds Busarello, G., Capaccioli, M. & Longo, G., Kluwer Academic Publishers, Dordrecht.
de Zeeuw, P. T. & Franx, M., 1991. *Ann. Rev. Astr. Astrophys.*, **29,** in press.
Djorgovski, S., 1985. *PhD thesis,* University of California, Berkeley (Dj).
Djorgovski, S. & Davis, M., 1987. *Astrophys. J.*, **313,** 59.
Djorgovski, S., de Carvalho, R. & Han, M. S., 1988. In: *The Extragalactic Distance Scale, ASP conf. ser., Vol. 4,* p. 329, eds van den Bergh, S. & Pritchet, C. J., ASP, San Francisco.
Dressler, A., Lynden-Bell, D., Burstein, D., Davies, R. L., Faber, S. M., Terlevich, R. & Wegner, G., 1987. *Astrophys. J.*, **313,** 42.
Faber, S. M., Dressler, A., Davies, R. L., Burstein, D., Lynden-Bell, D., Terlevich, R. & Wegner, G., 1987. In: *Nearly Normal Galaxies,* p. 175, ed. Faber, S. M., Springer-Verlag, Berlin.
Faber, S. M., Wegner, G., Burstein, D., Davies, R. L., Dressler, A., Lynden-Bell, D. & Terlevich, R., 1989. *Astrophys. J. Suppl.*, **69,** 763.
Fillmore, J. A., 1986. *Astr. J.*, **91,** 1096.
Franx, M., Illingworth, G. D. & Heckman, T. M., 1989a. *Astrophys. J.*, **344,** 613 (FIHa).
Franx, M., Illingworth, G. D. & Heckman, T. M., 1989b. *Astr. J.*, **98,** 538 (FIHb).
Franx, M., Illingworth, G. D. & de Zeeuw, P. T., 1991. *Astrophys. J.*, in press (FIZ).
Gradshteyn, I. S. & Ryzhik, I. M., 1980. *Tables of Integrals, Series and Products,* 6th edn, Academic Press, London.
Hernquist, L., 1990. *Astrophys. J.*, **356,** 359.
Jedrzejewski, R. I., 1987. *Mon. Not. R. astr. Soc.*, **226,** 747 (Je).
Jedrzejewski, R. I. & Schechter, P. L., 1989. *Astr. J.*, **98,** 147 (JS).
Kormendy, J., 1987. In: *Nearly Normal Galaxies,* p. 175, ed. Faber, S. M., Springer-Verlag, Berlin.
Lynden-Bell, D., Faber, S. M., Burstein, D., Davies, R. L., Dressler, A., Terlevich, R. & Wegner, G., 1988. *Astrophys. J.*, **326,** 19.
Merritt, D., 1985. *Mon. Not. R. astr. Soc.*, **214,** 25P.
Mihalas, D. & Binney, J. J., 1981. *Galactic Astronomy,* 2nd edn, Freeman, San Francisco.
Peletier, R. F., Davies, R. L., Illingworth, G. D., Davies, L. E. & Cawson, M., 1990. *Astr. J.*, **100,** 1091 (PDIDC).
Rybicki, G. B., 1987. In: *IAU Symposium 127, Structure and Dynamics of Elliptical Galaxies,* p. 397, ed. de Zeeuw, P. T., Reidel, Dordrecht.
Rix, H. W. & White, S. D. M., 1990. *Astrophys. J.*, **362,** 52.
Saglia, R. P., 1990. *PhD thesis*, Scuola Normale Superiore, Pisa, Italy.
Sandage, A. R. & Tammann, G., 1981. *A Revised Shapley-Ames Catalogue of Bright Galaxies* (RSA), Carnegie Institution, Washington DC.
Scorza, C. & Bender, R., 1990. *Astr. Astrophys.*, **235,** 49.
Statler, T. S., 1987. *Astrophys. J.*, **321,** 113.
Tonry, J. L., 1983. *Astrophys. J.*, **266,** 58.
van Albada, T. S., 1982. *Mon. Not. R. astr. Soc.*, **201,** 939.
van der Marel, R. P., Binney, J. J. & Davies, R. L., 1990. *Mon. Not. R. astr. Soc.*, **245,** 582 (Paper II).
van der Marel, R. P. & Cinzano, P., 1991. In: *Morphological and Physical Classification of Galaxies,* eds Busarello, G., Capaccioli, M. & Longo, G., Kluwer Academic Publishers, Dordrecht.

APPENDIX A: GEOMETRICAL FACTORS

This Appendix gives the function Ω and the geometrical factors α, β, γ and η that are used in Section 2.1. A system of spherical polar coordinates (r,θ,ϕ) is adopted. The z axis is the symmetry axis of the galaxy. The y axis lies in the plane of the sky. The positive y axis has $\phi=0°$. The inclination angle i is the angle between the z axis and the line of sight. Furthermore, (R,ϕ,z) are the usual cylindrical coordinates. Remember that in Section 2.1 σ_r^2, σ_θ^2 and $\overline{v_\phi^2}$ were assumed not to vary with position. According to these definitions

$$v_R = v_r \sin\theta + v_\theta \cos\theta, \qquad v_z = v_r \cos\theta - v_\theta \sin\theta. \tag{A1}$$

By assumption $\overline{v_r v_\theta}=0$. Taking the square of equations (A1) and calculating the density-weighted average over the system

yields equations (6), with

$$\eta \equiv \frac{\int \rho(\boldsymbol{r}) \cos^2\theta \, d^3\boldsymbol{r}}{\int \rho(\boldsymbol{r}) \, d^3\boldsymbol{r}}. \tag{A2}$$

Substitution of equation (5) yields

$$\eta = \frac{\int_0^1 [y^2(1-q_t^2)+q_t^2]^{-s/2} y^2 \, dy}{\int_0^1 [y^2(1-q_t^2)+q_t^2]^{-s/2} \, dy}. \tag{A3}$$

For $s=3$ and $s=4$ analytical expressions for η can be given [use equations (2.271.5) and (2.272.4) of Gradshteyn & Ryzhik (1980) for $s=3$ and equations (2.173.1) and (2.175.5) for $s=4$]. For $q_t \to 1$, $\eta \to 1/3$.

Let the line of sight pass through the point $(0, y_0, z_0)$. Define along the line of sight a coordinate $w = x \sin i + (z - z_0)\cos i$. The second moment of the line-of-sight velocity component in a particular point along the line of sight is then

$$\overline{v_l^2} = \overline{v_\theta^2} + \sin^2 i \cos^2\phi (\overline{v_\phi^2} - \overline{v_\theta^2}) + [(w + z_0 \cos i)/r]^2 (\overline{v_r^2} - \overline{v_\theta^2}). \tag{A4}$$

Expressions for the geometrical factors α, β and γ [equations (7)] are obtained by calculating the luminosity-weighted line-of-sight projection of $\overline{v_l^2}$, for lines of sight passing through the projected minor and major axis, respectively. Defining

$$\langle\langle f(w) \rangle\rangle (a,b,c) \equiv \frac{\int_{-\infty}^{\infty} (aw^2+bw+c)^{-s/2} f(w) \, dw}{\int_{-\infty}^{\infty} (aw^2+bw+c)^{-s/2} \, dw}, \tag{A5a}$$

this yields

$$\alpha = \left\langle\left\langle \frac{w^2 + 2w\cos i + \cos^2 i}{w^2 + 2w\cos i + 1} \right\rangle\right\rangle (q_t^2 \sin^2 i + \cos^2 i, 2\cos i, 1), \tag{A5b}$$

$$\beta = \left\langle\left\langle \frac{1}{w^2 + (1/\sin^2 i)} \right\rangle\right\rangle (q_t^2 \sin^2 i + \cos^2 i, 0, q_t^2), \tag{A5c}$$

$$\gamma = \left\langle\left\langle \frac{w^2}{w^2+1} \right\rangle\right\rangle (q_t^2 \sin^2 i + \cos^2 i, 0, q_t^2). \tag{A5d}$$

Analytical, but very cumbersome, expressions for α, β and γ can be given using e.g. Gradshteyn & Ryzhik (1980), equation (3.259.3), but α, β and γ are most conveniently calculated numerically.

The function $\Omega(q_t)$ defined in equation (4) is (e.g. Binney 1978)

$$\Omega = \frac{1}{2} \frac{\left(\frac{1}{\sqrt{1-e^2}} \frac{\arcsin e}{e} - 1 \right)}{\left(1 - \sqrt{1-e^2} \frac{\arcsin e}{e} \right)}, \qquad e^2 \equiv 1 - q_t^2. \tag{A6a}$$

for oblate bodies, and

$$\Omega = \frac{1}{2} \frac{\left[1 - \frac{1-e^2}{2e} \ln\left(\frac{1+e}{1-e} \right) \right]}{\left[\frac{1}{2e} \ln\left(\frac{1+e}{1-e} \right) - 1 \right]}, \qquad e^2 \equiv 1 - (1/q_t^2). \tag{A6b}$$

for prolate bodies.

APPENDIX B: OBSERVATIONS AND PREDICTIONS FOR SELECTED GALAXIES

In this Appendix the kinematical data and the predictions of the model are plotted for several selected galaxies. The bottom plot for every galaxy is the function $\nu(r)$ [equation (3)]. Solid curves are for $i = 90°$, dashed curves for $i = 60°$. If

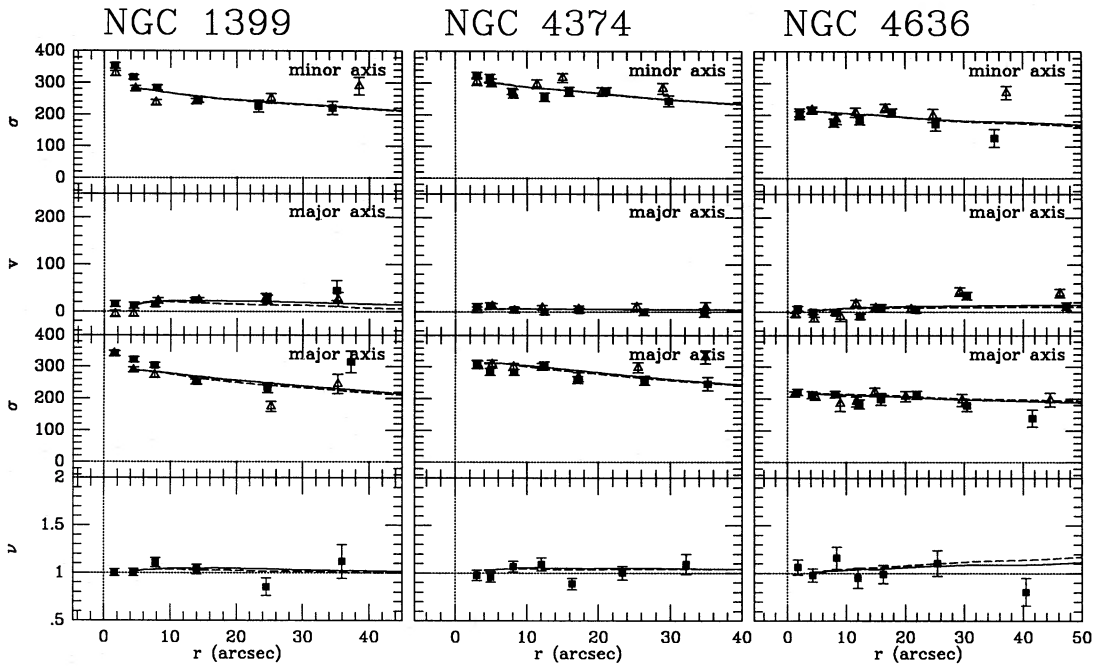

Figure 7a. Observations and predictions of oblate models for NGC 1399, NGC 4374 and NGC 4636. These are examples of galaxies with $v_{maj} > v_{min}$ for which our oblate models provide acceptable fits.

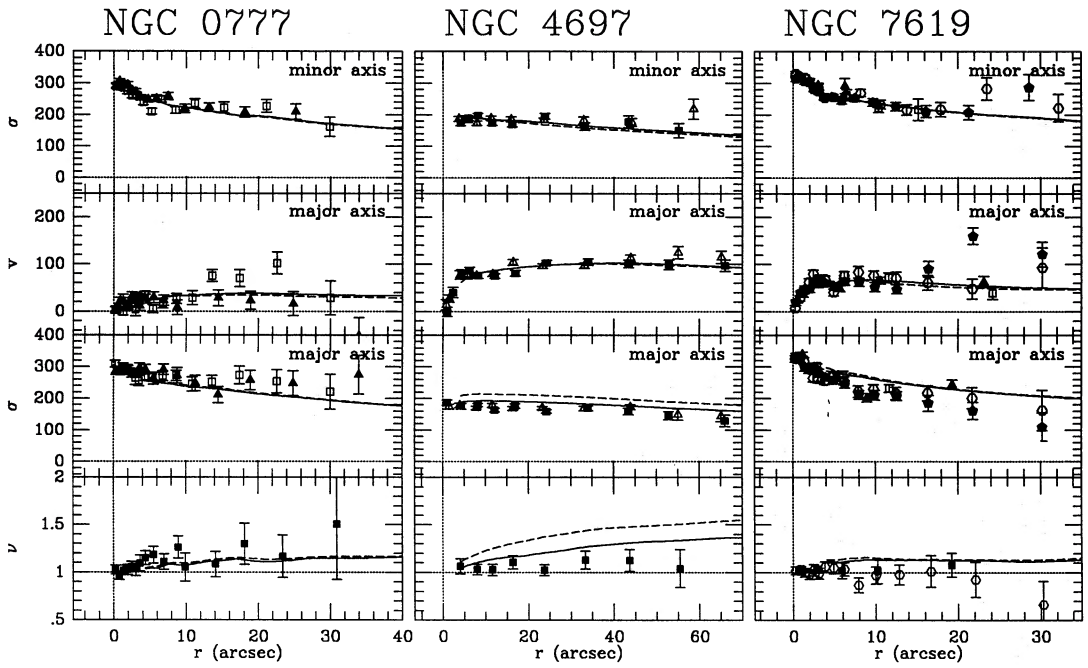

Figure 7b. Observations and predictions of oblate models for NGC 777, NGC 4697 and NGC 7619. These are examples of galaxies with $v_{maj} > v_{min}$ for which our oblate models cannot provide an acceptable fit. NGC 777 has $\bar{\mathscr{R}} < 1$, indicating either the presence of tangential anisotropy, or the presence of a disc component. NGC 4697 and NGC 7619 have $\bar{\mathscr{R}} > 1$, which indicates the presence of radial anisotropy. NGC 720 (Paper I) is an even more clear-cut example of a galaxy with $\bar{\mathscr{R}} > 1$.

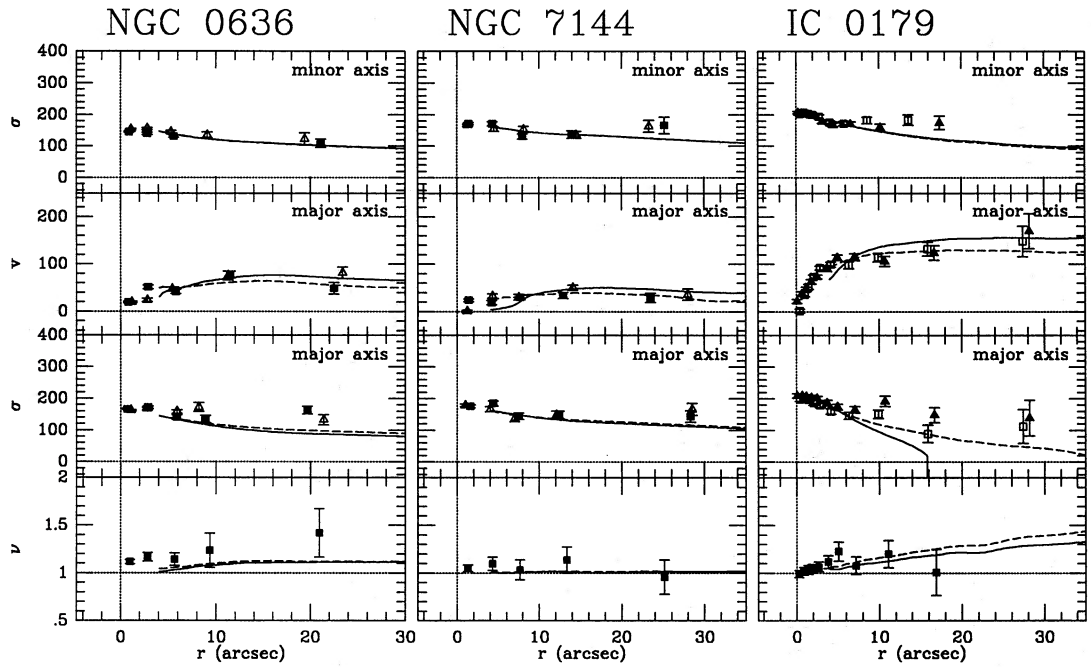

Figure 7c. Observations and predictions of oblate models for NGC 636, NGC 7144 and IC 179. These are examples of galaxies with $v_{maj} > v_{min}$ and $k > 1$. NGC 636 and IC 179 are probably misclassified S0s and cannot be well fitted by our models. NGC 7144 has a large isophote twist and is probably intrinsically significantly triaxial.

the dashed curves cannot be seen, they overlie the solid curves (which happens in models for galaxies with very low ε).

The data are presented as described in section 2.3 of Paper II. The errorbars plotted are the formal errorbars given by the source of the data. JS state that their formal errorbars are a factor 1.5 higher than is suggested by comparing different sides of the galaxy. Their formal errors are therefore multiplied by (2/3). The values plotted for $v(r)$ are calculated by taking together points that lie at comparable

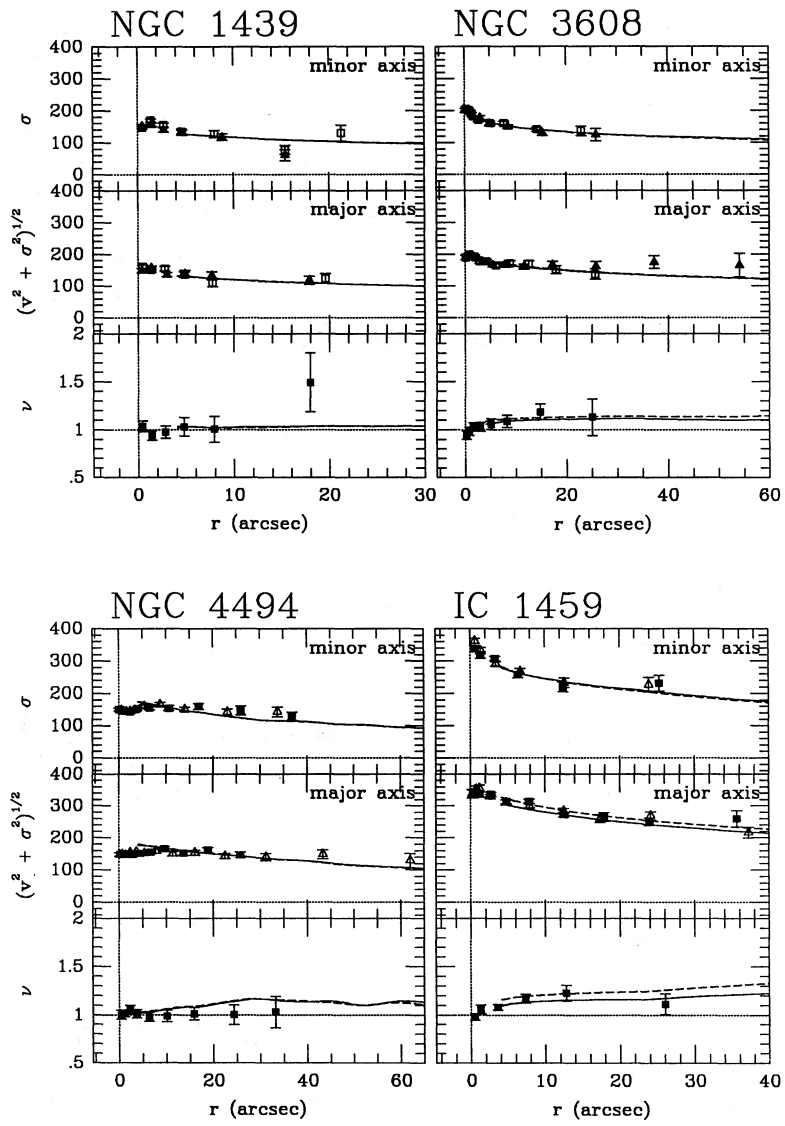

Figure 7d. Observations and predictions of oblate models for NGC 1439, NGC 3608, NGC 4494 and IC 1459. These are examples of galaxies with a peculiar major axis rotation curve (e.g. counter-rotating core; see the original sources of kinematical data). Except for NGC 4494, there is no evidence for peculiar behaviour in the quantity $v_{\rm rot}^2+\sigma^2$.

distances from the centre, using the definition in equation (3). In general every plotted point for $\nu(r)$ is thus a combination of eight independent datapoints: a rotation measurement and a dispersion measurement on either side of the nucleus and along both the major and the minor axis. The averaging of datapoints on different sides of the nucleus is done by calculating the weighted mean.

APPENDIX C: THE SCATTER IN THE $\Upsilon_R^{\rm imp}$ VERSUS M_B RELATION

The distances listed in Table 1 are derived from the $D_n-\sigma$ relation. In terms of the observed σ, μ, and flux f, the estimated distance $D_{\rm est}$ is obtained by equating $4\pi D_{\rm est}^2 f$ to the right-hand side of equation (14). In reality the FP has a finite thickness, due to intrinsic scatter in equation (16). Suppose that for a particular galaxy

$$(M/L)=C^{-0.75}KL^{0.25}\mu^{-0.01}(1+\varepsilon). \tag{C1}$$

Substitution in equation (15) then yields

$$L=C\sigma^{2.65}\mu^{-0.65}(1+\varepsilon)^{-1.32}. \tag{C2}$$

The true distance D is obtained by equating $4\pi D^2 f$ to the right-hand side of equation (C2). The estimate $\Upsilon_R^{\rm imp}$ (based on the distance $D_{\rm est}$) of the true mass-to-light ratio (M/L) satisfies $\Upsilon_R^{\rm imp}=(M/L)(D/D_{\rm est})$. From the above it follows that $(D/D_{\rm est})=(1+\varepsilon)^{-0.66}$. Substitution of equation (C1) then yields

$$\Upsilon_R^{\rm imp}=C^{-0.75}KL^{0.25}\mu^{-0.01}(1+\varepsilon)^{0.34}. \tag{C3}$$

Comparing this relation to equation (C1), it is concluded that

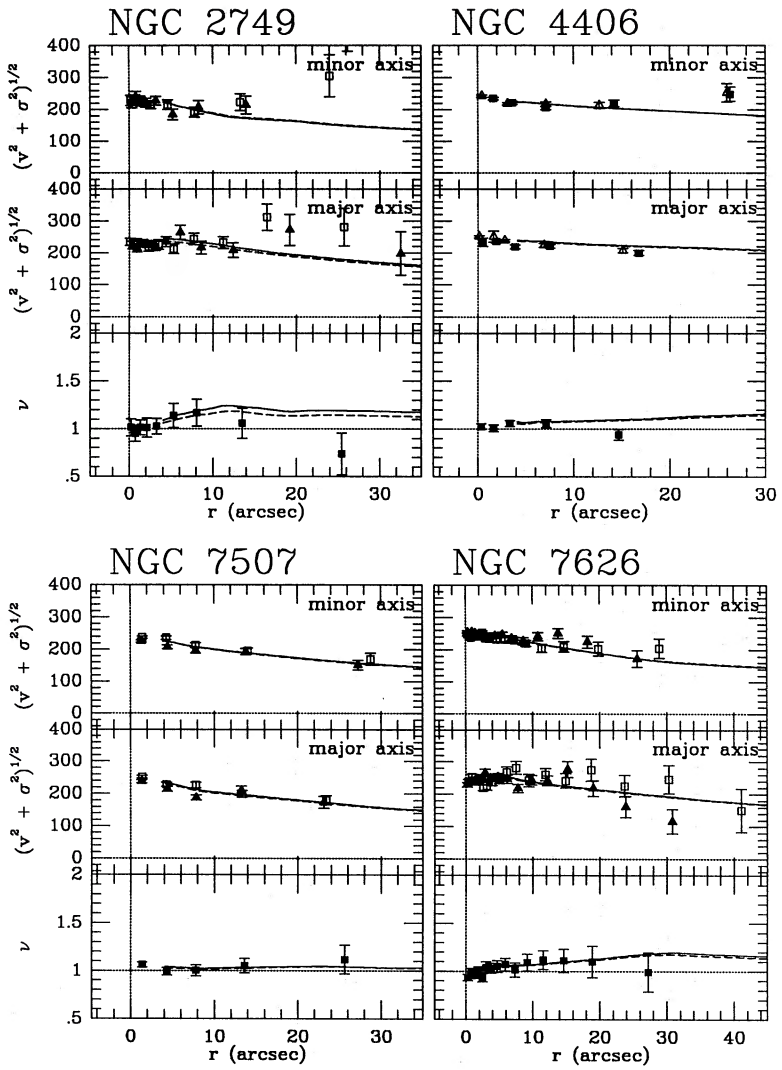

Figure 7e. Observations and predictions of prolate models for NGC 2749, NGC 4406, NGC 7507 and NGC 7626. NGC 4406 and NGC 7626 have a kinematically peculiar core component.

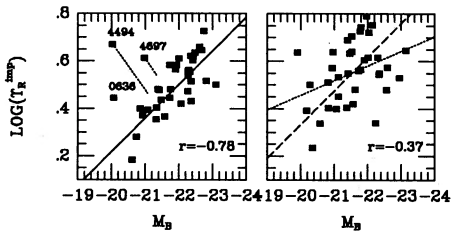

Figure 8. $\mathrm{Log}(\Upsilon_R^{imp})$ versus M_B, (a) using distances derived from the $D_n-\sigma$ relation (the same plot as Fig. 6a); (b) using distances $D_{est}=v_{gr}/H_0$ (see text). The dotted line is the best least-squares fit to the data. The dashed line is the best fit of a line with the same slope as the line in (a). The number in the bottom right corner is Pearson's *r*.

by using the $D_n-\sigma$ relation to estimate distances, one artificially reduces the *intrinsic* scatter around equation (16) by a factor ~ 3.

An alternative approach is to use distances $D_{est}=v_{gr}/H_0$, where v_{gr} is the group velocity corrected for motion of the Sun with respect to the centroid of the Local Group. The resulting relation between mass-to-light ratio and luminosity is plotted in Fig. 8(b), and differs from Fig. 8(a) in three ways: (i) the scatter has increased drastically; (ii) the slope of the best least-squares fit is closer to zero; and (iii) the average mass-to-light ratio of the sample is larger. In Fig. 8(b) however, a horizontal line (i.e. mass-to-light ratio independent of luminosity) is still excluded at the 2.5σ level. The differences compared to Fig. 8(a) are easily understood: (i) arises because all peculiar velocities are incorrectly interpreted as distance shifts; (ii) is a direct consequence of the increased scatter and the fact that peculiar velocities should not correlate with luminosity; and (iii) arises because the average peculiar velocity of the galaxies in the sample is not zero (Lynden-Bell *et al.* 1988). All this is entirely consistent with the earlier conclusion that by using $D_n-\sigma$ distances only the scatter in equation (16) is affected, and not the relation itself.